NMR studies on lipid-peptide co-aggregation between ganglioside-containing membranes and -synuclein

Fridolf, Simon

2022

Document Version:
Publisher's PDF, also known as Version of record

NMR studies on lipid-peptide co-aggregation between ganglioside-containing membranes and α-synuclein

SIMON FRIDOLF | DIVISION OF PHYSICAL CHEMISTRY | LUND UNIVERSITY

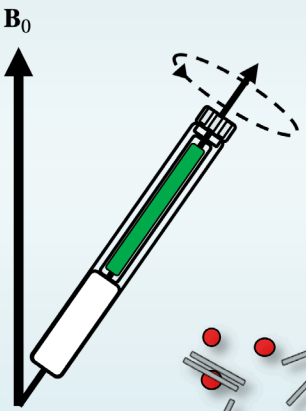

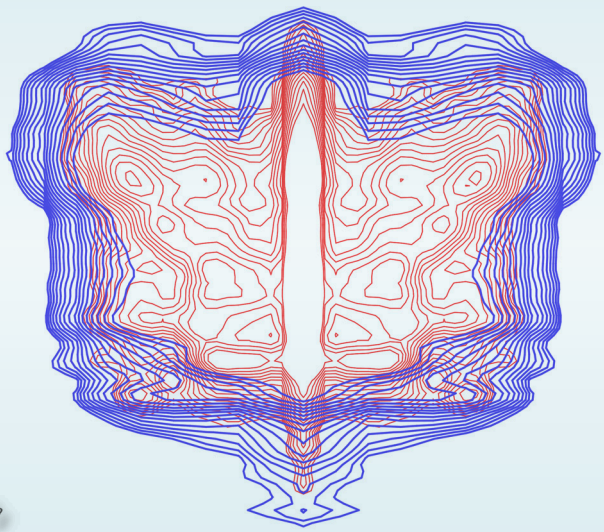

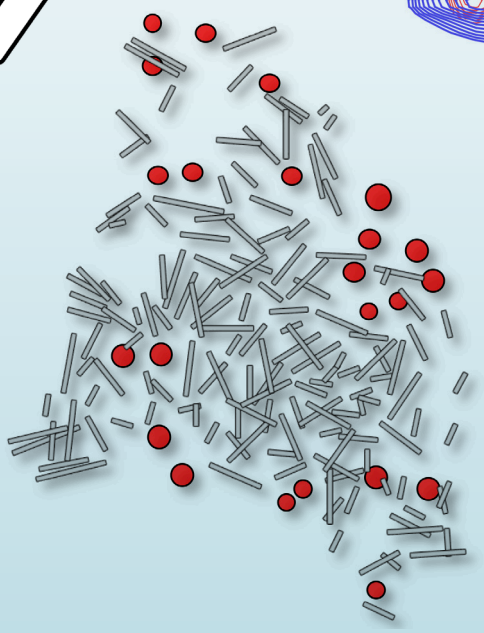

NMR studies on lipid-peptide co-aggregation between ganglioside containing membranes and α-synuclein

by Simon Fridolf

LUND
UNIVERSITY

DOCTORAL DISSERTATION

by due permission of the Faculty of Science, Lund University, Sweden.

To be defended on Friday, the 11th of November at 09:00 in the Lecture Hall C at the Department of Chemistry, Lund University.

Faculty opponent

Prof. Gerhard Gröbner

Umeå University, Sweden

Organization	Document name
LUND UNIVERSITY Department of Chemistry Box 124 SE-221 00 LUND Sweden	**DOCTORAL DISSERTATION** Date of disputation 2022-11-11
Author(s Simon Fridolf	Sponsoring organization Funding information could go here

Title and subtitle

NMR studies on lipid-peptide co-aggregation between ganglioside containing membranes and α-synuclein

Abstract

The aggregation of the protein α-synuclein and lipids in intracellular inclusions called Lewy bodies is the hallmark of Parkinson's disease, dementia with Lewy bodies and multiple system atrophy. In this thesis we investigated how the aggregation of α-synuclein is affected by lipid membranes that contain the glycolipid GM3, which belongs to the ganglioside class of lipids that have functions in cell signalling and regulation of processes at the membrane surface.

We studied the properties of the POPC-GM3 lipid system and aggregates that formed spontaneously between α-synuclein monomers and small unilamellar vesicles containing POPC and GM3 lipids at mildly acidic pH using nuclear magnetic resonance spectroscopy (NMR), molecular dynamics simulations, X-ray scattering and cryo-transmission electron microscopy. We also applied dynamic nuclear polarization (DNP)-enhanced NMR experiments to investigate the nm-structure of aggregates.

We found that a defining feature of the POPC-GM3 bilayer is the high order and slow dynamics in the oligosaccharide headgroup of GM3. We also found that the concentration of GM3 in vesicles correlates with the lipid fraction in μm-sized amorphous co-aggregates of lipids and α-synuclein fibrils. The lipids in aggregates are organized as adsorbed bilayers with reduced dynamics.

Key words

NMR spectroscopy, lipid membrane, α-synuclein, protein aggregation, lipid dynamics, ganglioside

Classification system and/or index terms (if any)

Supplementary bibliographical information		Language English
ISSN and key title		ISBN 978-91-7422-910-3 (print) 978-91-7422-911-0 (pdf)
Recipient's notes	Number of pages	Price
	Security classification	

NMR studies on lipid-peptide co-aggregation between ganglioside containing membranes and α-synuclein

by Simon Fridolf

LUND
UNIVERSITY

This doctoral thesis is constructed as a summary of research papers and consists of two parts. An introductory text puts the research work into context and summarizes the main conclusions of the papers. Then, the research publications themselves are reproduced. The research papers may either have been already published or are manuscripts at various stages.

Cover art: A R-PDLF type solid-state NMR spectrum of lipids.

Faculty of Science, Department of Chemistry, Division of Physical Chemistry

978-91-7422-910-3 (print)
978-91-7422-911-0 (pdf)

Printed in Sweden by Media-Tryck, Lund University, Lund 2022

Media-Tryck is a Nordic Swan Ecolabel certified provider of printed material. Read more about our environmental work at www.mediatryck.lu.se

MADE IN SWEDEN

Table of Contents

List of publications

This thesis is based on the following publications, referred to by their Roman numerals in the text:

I. **Ganglioside GM3 stimulates lipid-protein co-assembly in α-synuclein amyloid formation**
Simon Fridolf, Quoc Dat Pham, Jon Pallbo, Katja Bernfur, Sara Linse, Daniel Topgaard and Emma Sparr
In peer-review.

II. **Molecular dynamics simulations and solid-state nuclear magnetic resonance spectroscopy measurements of C-H bond order parameters and effective correlation times in a POPC-GM3 bilayer**
Simon Fridolf, Mona Koder Hamid, Leo Svenningsson, Marie Skepö, Emma Sparr, Daniel Topgaard
Accepted in Physical Chemistry Chemical Physics.

III. **Organization of lipids from ganglioside GM3 vesicles in α-synuclein co-aggregates**
Simon Fridolf, Leo Svenningsson, Katja Bernfur, Emma Sparr, Daniel Topgaard
Manuscript.

IV. **Proximity between natural moisturizers and components of the *stratum corneum* observed from dynamic nuclear polarization enhanced 2D ^{1}H-^{13}C solid state NMR with ^{1}H-^{1}H spin diffusion**
Leo Svenningsson, Simon Fridolf, Maria Gunnarsson, Arthur Pinon and Daniel Topgaard
Manuscript.

My contribution to the papers

Paper I: Ganglioside GM3 stimulates lipid-protein co-assembly in α-synuclein amyloid formation

I designed the experiments together with QDP, ES and DT. I did the sample preparation with help from KB and JP. I performed all the NMR experiments with help from JP. I performed the X-ray scattering experiments. I analyzed the NMR results with help from JP. I analyzed the X-ray scattering and cryo-TEM results. I wrote the paper together with ES and with feedback from the other co-authors.

Paper II: Molecular dynamics simulations and solid-state nuclear magnetic resonance spectroscopy measurements of C-H bond order parameters and effective correlation times in a POPC-GM3 bilayer

I did the sample preparation for the NMR experiments. I performed NMR experiments together with LS and DT. I analyzed the MD and NMR results together with MKH, LS and DT. I wrote the paper with feedback from the other co-authors.

Paper III: Organization of lipids from ganglioside GM3 vesicles in α-synuclein co-aggregates

I helped design the experiments with DT. I did the sample preparation with help from KB. I performed NMR experiments together with LS and DT. I analyzed the NMR results with help from LS and DT. I wrote the paper with feedback from the other co-authors.

Paper IV: Proximity between natural moisturizers and components of the *stratum corneum* observed from dynamic nuclear polarization enhanced 2D ^{1}H-^{13}C solid state NMR with ^{1}H-^{1}H spin diffusion

I prepared the lipid-αSyn samples. I performed NMR experiments on the lipid-αSyn sample with help from AP and LS. I helped LS analyze the NMR results.

Acknowledgements

First and foremost, I would like to thank my supervisors Daniel Topgaard and Emma Sparr for your support and scientific guidance during these years. It has been an honor to work with you.

I would like to thank all my co-authors, especially Dat Pham and Leo Svenningsson for everything NMR-related and Mona Koder Hamid for your work on the MD simulations. A special thanks also goes to Göran Carlström, for all the assistance with practical NMR.

A big thank you to all the interesting people I have met at the Division of Physical Chemistry, you have made these years of work enjoyable and special. In hindsight I realize how exciting and diverse this workplace has been.

Finally, I would like to thank all my family and friends for your support and especially Linnéa, Gabriel and Muffins for your patience during the period in which this book was written.

Popular science summary

This topic of this thesis is how the presence of biomembrane molecules affect the behavior of a protein related to Parkinson's disease in a simplified (compared to in the cell) model system.

Lipids are fat molecules that make up the biological barriers in our body that control transport of essential molecules in and out of the cell and create an environment where membrane proteins can perform their functions. Some types of lipids can also act as surface recognition molecules, which communicate with other molecules outside of the cell such as proteins, toxins and viruses. Lipids are amphiphilic, which is crucial for their functions. That they are amphiphilic means that they have a part that is hydrophilic (water-loving) and another part that is hydrophobic (water-hating). This leads to the formation of self-assembled lipid structures in water, where hydrophilic parts shield the hydrophobic parts from water. The lipid bilayer of cell membranes is an example of one such self-assembled structure.

Proteins are complex molecules that perform most of the functions in cells, such as promoting and regulating biochemical reactions. Proteins assume their 3-dimensional structure through self-assembly and finding the right structure is crucial for their function. In some cases, this process can be disturbed which can lead to pathological conditions. In the case of Parkinson's disease, the protein α-synuclein assembles into highly ordered fibrils which end up in characteristic, large aggregates called Lewy bodies. It is not known exactly how these aggregates affect disease, but emerging evidence suggests that the process is affected by the presence of lipid membranes. Because both lipids and proteins self-assemble into their functional forms, it is possible that they can also co-assemble into mixed lipid-protein aggregates with new properties, which may be important in understanding the progression into disease.

To investigate this type of lipid-protein aggregation process, we mainly used an experimental technique called nuclear magnetic resonance spectroscopy. This technique uses radiofrequency irradiation of a sample and exploits the magnetic properties of nuclei to gain information on the composition, dynamics and structure of molecules at the atomic level.

Abbreviations

αSyn	Alpha-synuclein
CP	Cross-polarization
CSA	Chemical shift anisotropy
DO	Dioleoyl
DM	Dimyristoyl
DL	Dilauroyl
DNP	Dynamic nuclear polarization
eDUMBO	Experimental decoupling using mind-boggling optimization
FID	Free induction decay
FT	Fourier transform
HETCOR	Heteronuclear correlation
INEPT	Insensitive nuclei enhanced by polarization transfer
MAS	Magic angle spinning
MD	Molecular dynamics
NeuAc	*N*-acetylneuraminic acid
NMR	Nuclear magnetic resonance
PC	Phosphocholine
PO	Palmitoyl-oleoyl
R-PDLF	R-type proton detected local field
RF	Radio frequency
SLF	Separated local field
SPINAL	Small phase incremental alteration
SUV	Small unilamellar vesicle
TEM	Transmission electron microscopy
ThT	Thioflavin T
TPPM	Two-pulse phase modulation

Introduction

This thesis is about the application of NMR spectroscopy to better understand how lipids interact with the protein α-Synuclein (αSyn), which is known to form characteristic insoluble deposits in Parkinson's disease. The focus is on the dynamical and structural properties of lipids and how the presence of the glycolipid GM3 influences the interaction between lipid membrane and aggregating protein. This section will provide a summary of the motivation for the thesis work.

Goal of the thesis

The goal of this thesis is to improve understanding on how the presence of lipid membranes containing ganglioside lipids affects the aggregation of the amyloid protein αSyn.

Protein misfolding and amyloid aggregation is associated with a collection of serious and well-known diseases including Alzheimer's and Parkinson's disease and type II diabetes.[1] Since the discovery that αSyn is one of the main components of inclusions called Lewy bodies in the substantia nigra of the brain during Parkinson's disease,[2] intense research has gone into trying to reveal the underlying molecular mechanisms. More recently, attention has been directed towards the interplay between αSyn and membrane lipids as a factor in αSyn aggregation. Lipids and dysfunctional membrane structures have been shown to be more prevalent in Lewy bodies than was previously known.[3]

It is in this setting with an increased focus on the interaction between the chemical properties of lipids and αSyn aggregation that work on this thesis began, with the overall goal to improve understand how the presence of the glycolipid GM3 in membranes affects the properties of αSyn aggregates, which may be viewed as lipid-protein co-aggregates as demonstrated by previous studies.[4-6] The main tool used in the thesis work was NMR spectroscopy, which due to the central role in this thesis will be more thoroughly described in the methods chapter.

NMR spectroscopy of lipid membranes

Most of the experimental work for this thesis was done using solid-state NMR spectroscopy. This experimental technique is non-invasive and exploits the interaction between radiofrequency pulses and the magnetic properties of nuclei in the presence of a constant and strong magnetic field generated by a superconducting magnet. This allows the operator to obtain information on the structure and dynamics of molecules containing for example ^{1}H, ^{13}C and ^{31}P. Solid-state NMR techniques are especially well-suited for the investigation of systems which are characterized by strong anisotropic interactions, for example lipid liquid crystals.

Lipid bilayers under physiological conditions are normally arranged in a liquid crystalline phase. Such a phase has dynamical properties like liquids with high diffusion rates and crystal-like structural properties with high spatial order. The orientations of lipids in a liquid crystalline bilayer are strongly correlated and the hydrophilic headgroups are directed towards water. The properties of lipid phases are described more in the background chapter. Much of the thesis work focuses on the dynamics of lipids, which regards information on how molecular segments move around in time.

Aims and outline

The overall goal was pursued by performing the work contained in papers **I**-**IV**, which are summarized here and more fully described in the chapter "Co-aggregation of ganglioside GM3 and α-Synuclein". The model system and research questions are summarized in Fig. 1.

In paper **I** we aimed to answer the questions:

- Is there an uptake of lipids from POPC-GM3 vesicles into αSyn aggregates?
- If there is lipid uptake, is it selective for POPC or GM3?
- Does the concentration of GM3 in the vesicles and the total lipid-to-protein ratio affect the composition of aggregates and supernatant?
- Does aggregation affect the dynamics of lipids?
- Does co-aggregation of POPC-GM3 vesicles with αSyn affect the aggregate morphology?

To answer these questions, we investigated the composition of lipid-αSyn aggregates with quantitative NMR analysis on the aggregates and the remaining solution (Fig. 1) while varying the GM3 concentration in vesicles and the total lipid-to-protein ratio to determine the effect of GM3 on total and specific lipid uptake.

We used solid-state NMR experiments and cryo-TEM imaging to investigate the lipid dynamics in aggregates and aggregate morphology respectively.

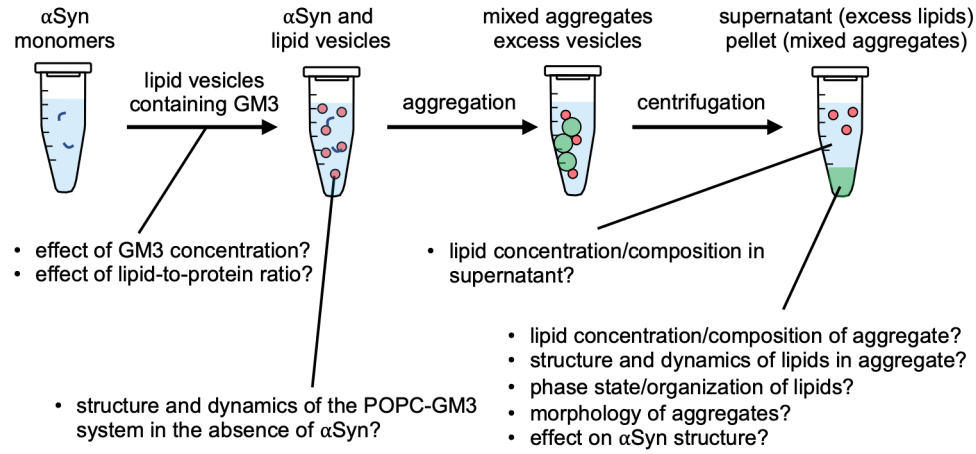

Figure 1
Grapical summary of the model system and research questions for papers **I-IV**. The sample preparation consisted of incubating αSyn monomers with POPC SUVs containing either 10 or 30 mol% of GM3. After aggregation had taken place, the precipitate and remaining supernatant were analyzed seperately. Samples of the lipid system in an equilibrium (non-sonicated) phase was also studied in the absence of αSyn.

In paper **II** we aimed to answer the questions:

- How does the presence of GM3 affect the atomic-scale structure and dynamics in a POPC bilayer?
- What is the defining feature that the presence of GM3 imposes on a POPC bilayer?

These are central questions for the thesis, as the presence of GM3 with a large oligosaccharide headgroup will likely modify the properties of the bilayer and may, in turn, affect the interaction between lipid vesicle and αSyn during aggregation. To investigate the effect of GM3, we used solid-state NMR to measure atomic-scale structure and dynamics in POPC bilayers without and with 30 mol% GM3. The same molecular parameters were obtained by performing MD simulations to complement the NMR results.

In paper **III** we aimed to answer the questions:

- How does co-aggregation of POPC-GM3 vesicles with αSyn affect the atomic-scale structure and dynamics of lipids?
- How are lipids organized in co-aggregates?

With the information from paper **II** in hand, we used solid-state NMR to investigate the same molecular parameters for lipids that were part of a lipid-protein aggregate with αSyn amyloid fibrils. We also used an additional solid-state NMR technique to investigate the average orientation of the POPC headgroup, to gain insight on how lipids are arranged in aggregates. In previous studies it has been speculated on how lipids in this type of aggregates are organized, for example as adsorbed vesicles, continuous layers of lipid on fibrils or αSyn surfaces or as dispersed lipids in the fibril structure. The type of organization may affect the thermodynamic or colloidal stability of aggregates.

In paper **IV** we aimed to answer the questions:

- What parts of lipids and αSyn are in close (nm) contact with each other and how far is the distance between them?
- How are lipids organized in co-aggregates (in higher detail than paper **III**)?

We used solid-state NMR techniques to investigate these questions for the same type of lipid-αSyn aggregates as in paper **III** and an additional system of stratum corneum (upper layer skin), where the latter is unrelated to this thesis. Because of technical limitations we were unable to answer the questions posed in paper **IV** for the lipid-αSyn system. However, the preliminary results that were produced can hopefully guide future research and are discussed in the conclusions chapter.

The outline of this thesis is as follows: in the background chapter, an overview of the physiochemical properties and behavior of the lipid and protein model system that was used in the thesis work is given together with its biological context. In the NMR methods chapter, the basic principles of solid-state NMR are presented together with the specific experimental techniques that were used to investigate the research questions stated above. In the co-aggregation of ganglioside GM3 and α-synuclein chapter, the main findings in papers **I**-**IV** are discussed, followed by an outlook section with suggestions for future work on the investigated systems.

Background

Amphiphilic molecules have parts that interact favourably with water and others that do not, which defines their behavior in aqueous solution. The self-assembly of both lipids and amphiphilic proteins are governed by the same physical principles. This chapter aims to provide some basic concepts that are useful for understanding the self-assembly of lipids and general features of colloidal systems in water. The chapter is based on the textbooks of Evans and Wennerström[7] and Mouritsen.[8]

Basic principles in colloidal systems

Demixing, surface energy and nucleation

The behavior of both lipids and aggregating proteins in solutions are in large part based on the hydrophobic effect, which causes lipids to phase separate and form lipid mesophases above a critical concentration and aggregating proteins to form a precipitate in water. These demixing effects are in a regular solution description rationalized by considering the free energy of mixing

$$\Delta G_{\mathrm{mix}} = (n_{\mathrm{A}} + n_{\mathrm{B}})[X_{\mathrm{A}} X_{\mathrm{B}} w + RT(X_{\mathrm{A}} \ln X_{\mathrm{A}} + X_{\mathrm{B}} \ln X_{\mathrm{B}})], \qquad (1)$$

where A and B are different molecules, n is the number of moles, X is the molar fraction, R is the gas constant, T is the temperature and the interaction parameter w is defined as

$$w = z_{\mathrm{b}} N_{\mathrm{Av}} (W_{\mathrm{AB}} - \tfrac{1}{2} W_{\mathrm{AA}} - \tfrac{1}{2} W_{\mathrm{BB}}), \qquad (2)$$

where z_{b} is the number of nearest neighbours, N_{Av} is Avogadro's number and W is the pair interaction energy. The regular solution model is valid for mixing of liquids when the mixing only affects the positional order at constant density. In this context W is analogous to the enthalpy of vaporization, but with opposite sign. Lipids and aggregating proteins are not simple liquids, but Eq. 1 can still be used to rationalize why demixing occurs.[9] Recent reports have described aggregation of αSyn as a liquid-liquid phase separation process.[10, 11]

There are three parts of Eq. 1, a prefactor with the total number of moles and a term for the enthalpy and entropy respectively. In this model the entropy is always negative for a mixture, which favors mixing and reaches a minimum for the equimolar mixture when $X_A = X_B$. The enthalpy term can be negative or positive depending on the relative values of the heterogeneous and homogeneous interaction energies. If the average homogeneous interaction is stronger (more negative) than W_{AB}, the sign of w is positive which opposes mixing. In the case of lipid molecules in water, demixing occurs rapidly due to the insolubility of the hydrocarbon chains and self-assembly takes place.

Surface tension is a phenomenon associated with the imbalance of favourable interactions at a surface, for example water has high surface tension because of the strong interactions in the bulk water phase compared to the water-air interaction at the surface. When w in Eq. 2 is positive (the homogeneous interactions are more favorable), the exchange of homogeneous for heterogeneous interactions when a molecule if transferred to the surface leads to an increased internal energy of the system. The surface tension is defined in terms of the Gibbs free energy G as

$$\gamma = \left(\frac{\partial G}{\partial A}\right)_{T,P} \tag{3}$$

where A is the surface area created at constant temperature and pressure. Some behaviours of colloidal systems such as the spreading of one component on another and the nucleation of a new phase are readily conceptualized using γ. In the case of the nucleation of a new phase, for example an amyloid fibril, a surface tension term will oppose the formation of the new phase even when it is the lowest energy state. This leads to a sluggish behavior where supersaturated conditions are needed for nucleation. It has been shown that lipid membranes can promote primary nucleation of αSyn by stimulating primary nucleation,[12] which implies that the protein-lipid surface tension is lower than the protein-water surface tension which leads to a local increase in the αSyn concentration at a vesicle surface.

Forces and stability of colloidal systems

Forces between particles can be attractive or repulsive. In colloidal systems these are mainly described as electrostatic forces (attractive or repulsive), dispersion forces (attractive) and other forces of repulsive entropic origins. In the case of electrostatic interactions, the attractive force between two ions is described by Coulomb's law

$$F_{el,ion} = k_e \frac{q_1 q_2}{r^2} \tag{4}$$

where k_e is Coulomb's constant, q_1 and q_2 are the charges of the two ions and r is the distance between the ions. The force per area between two particle surfaces is described in Derjaguin-Landau-Verwey-Overbeek (DLVO) theory as

$$\frac{F_{\text{surfaces}}}{A} = \frac{-H_{121}}{6\pi h^3} + 64kTc_0^*\Gamma_0^2 \exp(-\kappa h) \qquad (5)$$

where H_{121} is the Hamaker constant that describes the attractive dispersion forces through an intervening medium (in this case solvent), kT is the thermal energy, c_0^* is the bulk ion concentration, Γ_0 is a factor defined by the surface charge density, κ is the inverse Debye length and h is the distance between particles. The attractive dispersion term in Eq. 5 becomes dominant at very large and small distances. At intermediate distances an electrical double-layer force leads to a potential energy barrier on the length scale of the Debye length. In the living cell, molecular crowding leads to a more complicated view than described above, which is the subject of a recent and excellent paper by Wennerström et al.[13]

In paper **II**, MD simulations were used to calculate lipid properties for comparison with NMR results. In this type of simulation, the molecular positions as a function of time are obtained by integrating Newton's second law of motion[14]

$$\frac{\mathrm{d}^2\mathbf{a}_i(t)}{\mathrm{d}t^2} = \frac{1}{m_i}\sum_{i<j}^{M}\mathbf{F}_{ij}(r_{ij}(t)) \qquad (6)$$

where $\mathbf{a}_i(t)$ and m_i is the acceleration and mass of molecule i, and $\mathbf{F}_{ij}$ and $r_{ij}(t)$ is the force and distance between particles i and j. A defined starting position for each molecule is then updated at different time steps during the simulation trajectory by evaluating Eq. 6. The forces between molecules described by $\mathbf{F}_{ij}$ are defined by interatomic potentials in models called force fields. These models are semi-empirical and contain terms corresponding to bonded and non-bonded interactions. Bonded terms describe the distortion of bond lengths and angles, while non-bonded terms are usually limited to electrostatic and van der Waals potentials.

It is not apparent that the above procedure will produce a realistic result because atoms are more accurately described by the laws of quantum mechanics, which are computationally expensive. But with validation from experiments and tuning of force fields, MD simulations can provide an atomic-resolution picture of molecular mechanisms. Because NMR spectroscopy also provides in-principle atomic resolution, the use of MD simulations is synergistic because these two methods report on the same type of atomic-scale information. However, there are some limitations to interpretation of NMR results using a validated MD simulation. The simulation is on a much smaller scale, both in the number of molecules in the sample and the timescale of the trajectory compared to an NMR experiment. This can lead to underestimation of large-scale collective effects and contributions from slower

motions to the overall dynamics in a lipid membrane, which are observable with NMR.

Self-assembly of lipid bilayers

Due to their amphiphilic nature which causes spontaneous orientation of hydrophilic and hydrophobic parts towards and away from water respectively, lipids have evolved to perform their biological functions from self-assembled aggregates. In biological systems bilayers are formed, which are sheets two molecules thick with a hydrocarbon interior and hydrophilic headgroup surface. This section describes some important properties of these structures, which are highly relevant for the behavior of the model system employed in the thesis work.

The lipid membrane

A eukaryotic plasma membrane is a highly complex assembly of lipid, protein and carbohydrate. It performs many important functions such as mediating transport to the cell by acting as a diffusion barrier and by providing active transport with the help of membrane protein channels or via endo- and exocytosis of vesicles. The membrane environment also acts as a solvent for proteins which carry out a wide variety of functions including immunological response, cell signalling and enzymatic catalysis. The plasma membrane is structured into three distinct layers with a lipid bilayer at its core. Facing the extracellular space is a polysaccharide layer called the glycocalyx and towards the cytosol a network of proteins forms the cytoskeleton.

The lipid diversity of the bilayer component is high and eukaryotic cells can contain several hundred different kinds of lipids. Some types of lipids are more common (Fig. 2), for example phosphocholines and cholesterol in the outer leaflet and phosphoserine or phosphoethanolamine in the inner leaflet of the lipid membrane. Other types of lipids can be less common on average but concentrated in certain tissues where they perform specialized functions. For example ganglioside[15] glycolipids which have large carbohydrate headgroups are concentrated on the outer leaflet of the plasma membrane, for use in molecular surface recognition. The lipid composition affects the properties of the membrane, for example unsaturations in the hydrophobic parts increases fluidity of the membrane and a large lipid headgroup size can increase the curvature of the bilayer. The net charge of the headgroup and the resulting surface charge density also has important consequences for interaction with other biomolecules and colloidal stability in the cell.

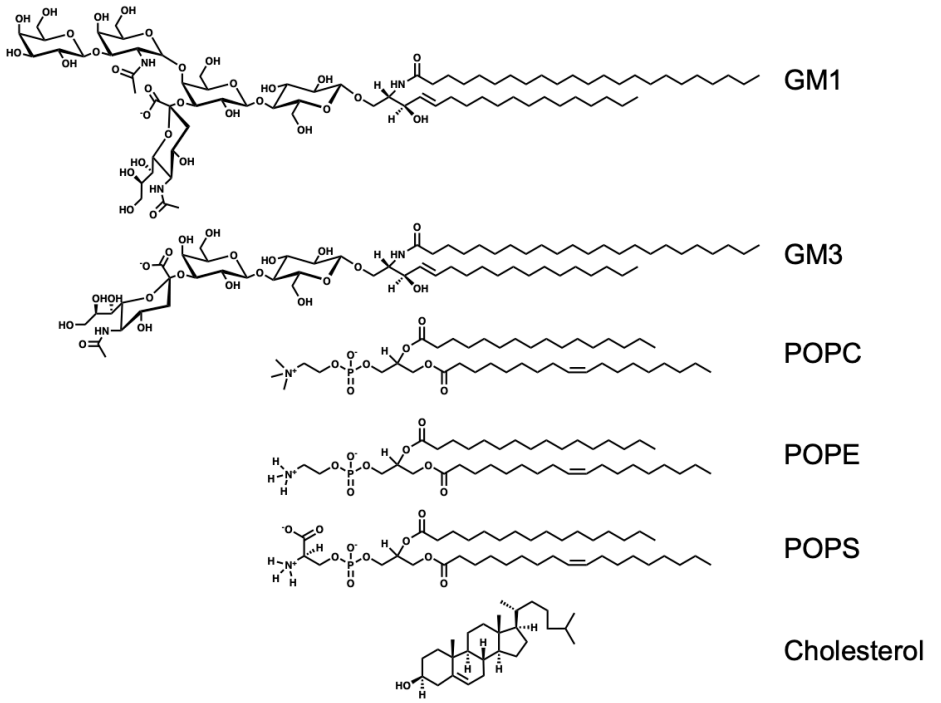

Figure 2
Different types of lipids in cellular membranes. Cholesterol, POPC and POPE are neutral or zwitterionic, while POPS, GM3 and GM1 have net negative charge. In terms of the packing parameter, cholesterol and the gangliosides are opposites of each other, with respectively small and large hydrophilic headgroups compared to the hydrophobic moiety.

Lipid polymorphism and aggregate structure

Bilayers can self-assemble into aggregates with different geometries depending on the lipid composition. While the driving force for self-assembly is the insolubility of the hydrophobic parts, repulsion between headgroups and packing of the hydrocarbon chains will lead to a preferential aggregate shape. The surfactant parameter n_s can be used to rationalize the aggregate shape[16]

$$n_s = \frac{v}{la} \qquad (7)$$

where v and l are the volume and length of the hydrophobic tails respectively and a is the effective headgroup size. The value of a depends on the type of polar headgroup and the corresponding sensitivity to changes in temperature and ionic strength of the solution. The relationship between n_s and aggregate structure can be illustrated by comparing POPC and GM3 in Fig. 3. For POPC the hydrophobic and

hydrophilic parts are similar in size with $n_s \approx 1$, which favours planar structures with no spontaneous curvature (Fig. 3A). In this context the curvature is often expressed as the mean curvature

$$H = \frac{1}{2}\left(\frac{1}{R_1} + \frac{1}{R_2}\right) \tag{8}$$

where R_1 and R_2 are radii of curvature for a point on the bilayer. For a planar bilayer $R_1 = R_2 \approx 0$, which results in $H \approx 0$. In the case of GM3 the headgroup area is larger while the hydrophobic part is only slightly larger than for POPC (for commercially available GM3 extracts) with $n_s < 1$. For this reason, GM3 spontaneously forms unilamellar vesicles where $H \neq 0$ (Fig. 3B).[17] Ganglioside GM1 which has a larger headgroup than GM3 forms micelles with even greater mean curvature (fig. 3C). Vesicles and micelles are approximately spherical which means that $R_1 = R_2 = R$, where R is the radius of the aggregate. Consequently, micelles which typically have smaller radii than vesicles also possess greater mean curvature. For larger vesicles, the curvature is typically close to zero.

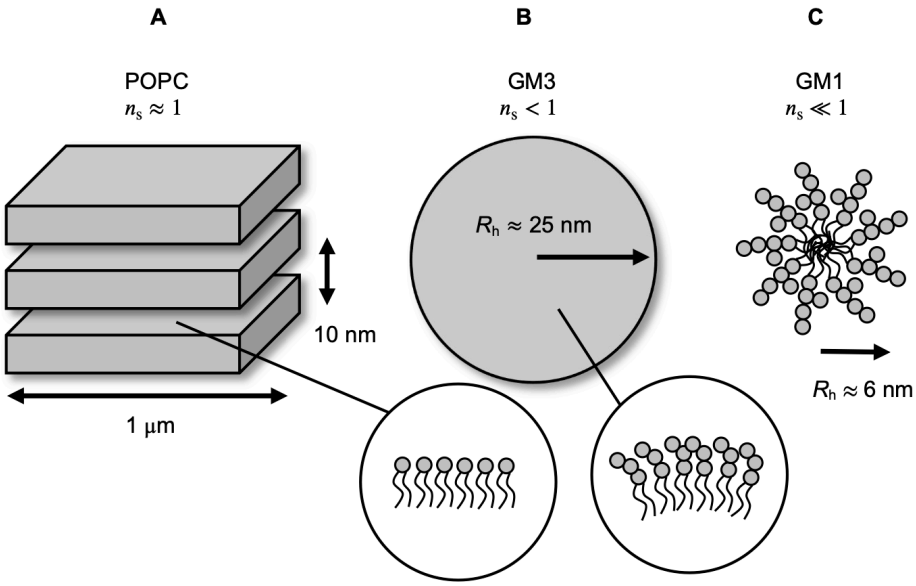

Figure 3
The packing parameter n_s and self-assembled lipid aggregate morphology. (**A**) POPC has similarly sized headgroup and hydrophobic parts, which results in $n_s = 1$ and a tendency to form lamellar phase with zero mean curvature H. (**B**) Lipids with slight larger headgroup than hydrophobic part $n_s < 1$ such as ganglioside GM3 spontaneously form small vesicles which have positive mean curvature $H > 0$. (**C**) Lipids with large headgroup compared to the hydrophobic part such as GM1 have $n_s \ll 1$ and spontaneously form micelles with higher mean curvature $H_{\text{micelle}} > H_{\text{vesicle}}$.

From the principles above, for a mixture of lipids with different n_s the resulting aggregate will have intermediate properties compared to the pure components. Depending on the mixing ratio, lipids with large headgroups like gangliosides can induce curvature on a mixed membrane with POPC. It has been proposed that release of curvature stress associated with morphological changes in bilayer structure can be an important mechanism in how membranes and peripheral proteins communicate.[18]

Lipid dynamics in bilayers

A liquid crystalline lipid bilayer is a lively environment with a hierarchy of motions on a range of time scales (Fig. 4). There typically exists a distinct hierarchy of molecular motions in the bilayer, from internal motions that reorient individual bonds (bond rotation, trans-gauche isomerization) to whole-lipid motions that reorient individual lipid molecules (axial rotation, wobble, protrusion, lateral diffusion and flip-flop) to collective motions that reorients the surface normal of the entire bilayer (bending, undulations and thermally excited viscoelastic deformations). The rates of these motions are generally a function of pressure, temperature and the phase state of the bilayer. Below the melting point of the lipid, lipid molecules are arranged in a gel phase with solid hydrophilic chains, while above the melting point the molecules are arranged in a liquid crystalline phase with mobile chains.

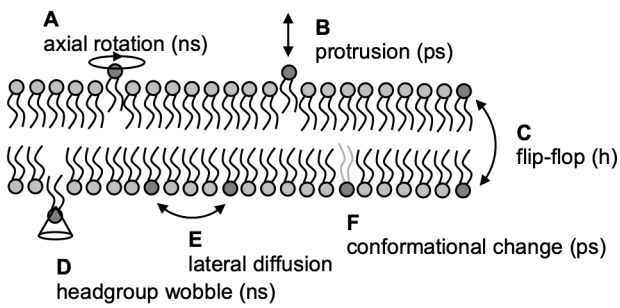

Figure 4
Examples of types of motions in liquid crystalline lipid bilayers. Additional modes of motion are mentioned in the text. (**A**) Rotation around the long axis of the lipid molecule. (**B**) Protrusion in and out of the bilayer. (**C**) Flip-flop motions between the inner and outer leaflet of the bilayer. (**D**) Wobbling of the lipid headgroup in a conical pattern. (**E**) Lateral diffusion in the bilayer plane. Typical diffusion coefficients are on the order of 10^{-11} m^2/s for POPC lipids, which is 100 times slower than free diffusion of water at 298 K. (**F**) Conformational change of the hydrophobic tails.

Lipid molecules in liquid crystalline bilayers are constantly performing librations (fast, oscillatory changes in orientation) and protruding small distances back and forth on the time scales of fs-ps. Rotation of C-H bonds and trans-gauche

isomerization are also rapid and occur on the ps time scale. Axial rotation of individual lipids occurs on the ns time scale, together with conical wobbling of the headgroup and acyl chains. The rotational diffusion of the headgroup and acyl chains of POPC has recently been shown to be decoupled from each other from NMR experiments.[19] The rate of lateral diffusion in the plane of the bilayer is typically described using a diffusion coefficient, which is on the order of 10^{-11} m^2/s for liquid crystalline bilayers. Flip-flop motions refer to the movement of a lipid between the two bilayer leaflets and is typically very slow because of the free energy penalty associated with transferring the polar headgroup through the hydrophobic interior of the bilayer. The function of a lipid membrane is likely linked to the complex coupling of all these fast motions and slower collective motions as illustrated by the "dynamic landscape" of POPC in the liquid crystalline state.[20]

The time scale of motions can be described using an autocorrelation function $g(\tau)$, which contains information on the time scale that stochastic processes randomize the orientations of molecular segments. For fast motions the correlation is lost rapidly with a corresponding rapid decay of $g(\tau)$. For slow motions the situation is the opposite. In lipid liquid crystalline bilayers, a set of motions on different time scales are superimposed on each other as described above. In this complex situation it is useful to define an effective correlation time τ_e for C-H bond rotational diffusion

$$\tau_e = \int_0^\infty \frac{g(\tau)-S_{CH}^2}{1-S_{CH}^2}\,d\tau, \qquad (9)$$

where S_{CH}^2 is the square of the C-H order parameter defined as

$$|S_{CH}| = \langle P_2(\cos\theta)\rangle = \langle\frac{3\cos^2\theta-1}{2}\rangle \qquad (10)$$

where θ is the angle between the C-H bond and the external magnetic field $\mathbf{B}_0$ that is present during NMR experiments and P_2 is the second-order Legendre polynomial. The quantities τ_e and $|S_{CH}|$ are defined in relation to $g(\tau)$ and interpreted molecularly in Fig. 5. During the thesis work τ_e and $|S_{CH}|$ were investigated both qualitatively using CP and INEPT intensities[21] and quantitatively using NMR dipolar and relaxation experiments. These methods are described more in the NMR methods chapter.

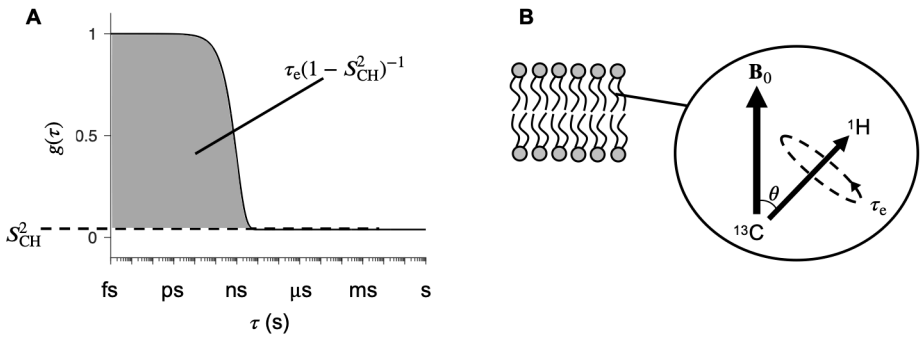

Figure 5
The C-H order parameter $|S_{CH}|$ and the effective correlation time τ_e. (**A**) For systems where the C-H motion is anisotropic, some orientations have very low probabilities which means that the autocorrelation function $g(\tau)$ reaches a plateau value of S^2_{CH} instead of rapidly decaying towards zero. The value of $|S_{CH}|$ is thus a measure of the degree of spatial restriction of motion.[22] The value of τ_e describes the rate of motions and is defined as the area between $g(\tau)$ and the plateau value S^2_{CH}, scaled by $(1 - S^2_{CH})^{-1}$. (**B**) Molecular interpretation of $|S_{CH}|$ and τ_e. The value of $|S_{CH}|$ is defined by the time-average angle θ between the C-H bond vector and the external magnetic field $\mathbf{B}_o$ (Eq. 10). The value of τ_e defines the time scale of C-H rotational motion at a given value of $|S_{CH}|$.

Ganglioside lipids

Structure and biology of gangliosides

Gangliosides are sialic acid-containing glycosphingolipids, which were linked to transmission of membrane-mediated information 50 years ago.[23] The structure of gangliosides include ceramide as the hydrophobic part and variable oligosaccharide headgroups containing combinations of the sugars glucose, galactose, *N*-acetylgalactosamine and *N*-acetylglucosamine and negatively charged *N*-acetylneuraminic acid (NeuAc).[24] The large negatively charged oligosaccharide headgroups of gangliosides suggest that they will impose curvature on a mixed membrane. The headgroup can also potentially provide opportunities for interactions with other charged molecules or the surrounding water molecules via electrostatic interactions or hydrogen bonding respectively.

Gangliosides are primarily located in the outer leaflet of the plasma membrane, with the headgroup extending from the membrane which provides the ability for functions in cell recognition and regulation of processes at the membrane surface, including membrane protein regulation.[25] Gangliosides are particularly concentrated (up to 10 wt%) in neurons.[26] Only four types of gangliosides (GM1, GD1a, GD1b and GT1b) make up 97% of the ganglioside content in the adult human brain. These major brain gangliosides are all biosynthesized via the common precursor ganglioside GM3, which is mainly concentrated in non-neuronal tissues.

Ganglioside GM3 has been shown to have a strong effect on the kinetics of αSyn aggregation[27, 28] and to become concentrated in the blood plasma during Parkinson's disease.[29] Because of the links between GM3 and αSyn aggregation, GM3 was chosen as part of the lipid model system in the thesis work. It is also convenient to use GM3 as a ganglioside model instead of the more complex gangliosides because the simpler structure of GM3 leads to less complex NMR spectra.

Deposition of α-synuclein aggregates

αSyn is a small 140 kDa protein mainly localized to the presynaptic terminus in neurons. It is one of the most abundant proteins in the brain and is proposed to have functions at the synapse with regulating synaptic vesicle pools and neurotransmitter release.[30] In the context of this thesis, αSyn was studied because of the link between lipids and Parkinson's disease which will be described more in this section.

Deposition of α-synuclein and amyloid disease

The first discovery and naming of αSyn is from its presence on synaptic vesicles and nuclear envelopes in the electric organ of torpedo ray.[31] Since then, αSyn has been identified as the main component of intracellular inclusions called Lewy bodies, which are characteristic for Parkinson's disease and dementia with Lewy bodies.[2] The Lewy inclusions are composed of a mixture of cellular matter, including proteins, crowded organelles and lipid membranes. In the case of Parkinson's disease, the link with αSyn has gained much attention after the finding that some mutations in the αSyn gene coincides with the familial form of the disease.[32] The links to Parkinson's disease and the presence of αSyn in Lewy body aggregates prompted intense research on the conformational changes into amyloid fibrils and aggregation of αSyn. Some proposed mechanisms behind cell death are mechanical distortion of cellular compartments, for example mitochondria, toxic gain of function or toxic loss of function. In the two latter, misfolding or conformational change leading to aggregation either produces toxic forms of αSyn such as oligomers[33] or depletes the pool of functional αSyn.[34]

Current knowledge has not been able to deliver a definitive conclusion on how αSyn might cause disease or cause nerve cells to die, however there is a growing collection of evidence that oligomers are able to damage lipid membranes.[35, 36] Another recent perspective is that not αSyn aggregation, but rather the subsequent formation of Lewy bodies might disrupt cellular functions.[37]

Physical chemistry of α-synuclein aggregation

The amino acid sequence of αSyn is shown in Fig. 6. The sequence is 140 amino acids long and is normally divided into three regions: N-terminus region (residues 1-60), central region (residues 61-95) and the C-terminus region (residues 96-140). These regions contain large fractions of positively charged residues (N-terminus), hydrophobic residues (central region) and negatively charged residues (C-terminus).

The native conformation of αSyn is intrinsically disordered both *in vitro* and *in vivo*, which means that it has no well-defined secondary structure. The aggregation into fibrils leads to a well-defined cross-β structure that is characteristic for amyloids.[38] The driving force for aggregation is the hydrophobicity of the central region, just like in the self-assembly of lipids. However, the situation with αSyn is more complex because it does not just have hydrophilic and hydrophobic ends like a lipid, but rather has two hydrophilic ends and a hydrophobic core. Electrostatic stabilization is normally viewed as an important mechanism for maintaining a resistance against aggregation for nano-sized particles and in the crowded intracellular environment.[13] In the case of αSyn, the conformational change from soluble monomer into oligomers and amyloid fibrils is highly dependent on solution conditions.[39] αSyn has an isoelectric point of 4.7 and changing the pH in the range of 4.0-7.4 has a large effect on aggregation kinetics. A reduction in pH typically increases the aggregation rate by enhancing secondary nucleation compared to elongation at pH 6.0,[40] acting as a mechanistic switch. Because of this mechanistic switching, the effect of changing the ionic strength depends on the pH of the solution. At low pH where secondary nucleation is the dominant mechanism addition of salt is proposed to retard aggregation because of the weakening of an attractive electrostatic component between the positively charged N-terminus of the αSyn monomer and the negatively charged C-termini on the growing aggregate surface.[41] At neutral pH the dominant growth mechanism is elongation of the fibril ends. It is important to keep in mind that the rate limiting step in αSyn aggregation can also be primary nucleation, which is typically very slow. For this reason, many studies use means to promote primary heteronucleation, such as addition of catalytic surfaces in the form of pre-formed seeds or inorganic beads, or mechanical agitation. Lipid phases are of special interest in the context of accelerating αSyn aggregation because of their biological relevance related to the role of αSyn in vesicle handling and will be described in the next section.

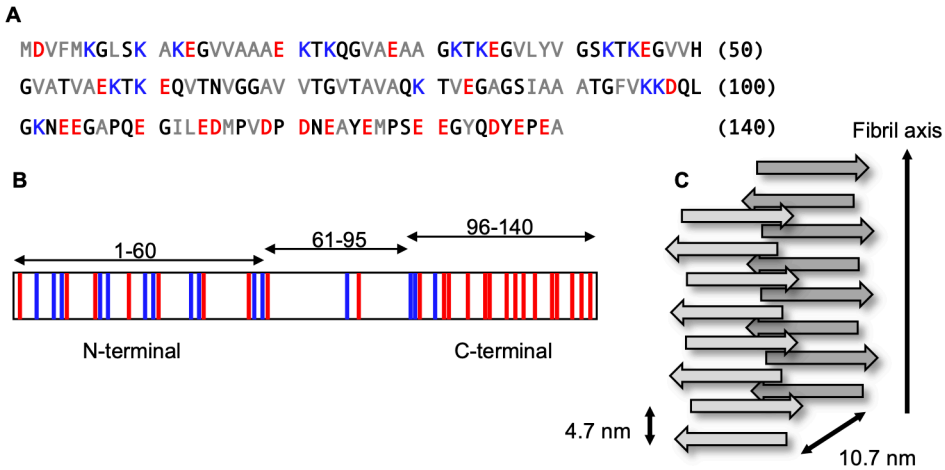

Figure 6
Structure of αSyn. (**A**) Primary amino acid sequence of αSyn. Color coding: red (acidic), blue (basic), grey (hydrophobic) and black (other). (**B**) Illustration of the uneven charge distrubution in αSyn. (**C**) Schematic illustration of the amyloid cross-β fibril conformation.

Co-aggregation of lipids and α-synuclein

When αSyn aggregates in the presence of lipids, there is a potential to form mixed aggregates which may have new properties compared to the individual αSyn and lipid components. The probability for this must be viewed as considerable because of the abundance of lipid surfaces and molecular crowding in the cell. This section will describe how interaction with lipids affects αSyn aggregation and the properties of co-aggregates.

Interactions between lipids and soluble α-synuclein

While αSyn monomers have no well-defined secondary structure, binding to anionic lipid membranes or sodium dodecyl sulphate micelles causes the N-terminus region to adopt a helical conformation.[42, 43] It was shown from NMR experiments that the three regions of αSyn have distinct roles in membrane binding, where the helical N-terminus acts as a membrane anchor, the central region determines the affinity of membrane binding and the C-terminus region is left unstructured and only weakly associated with the membrane.[44] The adoption of a helical structure is only observed for binding to negatively charged lipid membranes, which implies that the role of electrostatic interactions is important in how αSyn associates with membranes. Because of the uneven charge distribution in αSyn, an attractive interaction between

the positively charged N-terminus and a negatively charged membrane surface can be expected to promote membrane association, while a repulsive interaction between the negatively charged C-terminus and the membrane has the opposite effect. These two opposite effects could have a regulatory effect by modulating the affinity of αSyn for the membrane.

Hydrophobic interactions also contribute to the balancing of the affinity of αSyn for lipid membranes and it has been observed that αSyn binding to model membranes is much more prominent for lipids in a fluid rather than a gel phase.[45] This can be rationalized by considering the exposed hydrophobic area, which is larger for fluid membranes than for membranes in a gel phase.

Effect of lipids on α-synuclein aggregation

Amyloid fibril formation can be promoted by lipid membranes via effects on the protein conformation, orientation or by increasing the local concentration.[46] Several studies report a clear effect of lipid vesicles on the rate of αSyn aggregation by employing ThT binding assays.[47] The ThT molecule specifically binds to the cross-β structure that is characteristic for αSyn- and other amyloid fibrils, which leads to increased fluorescence intensity during aggregation. Experiments of this type has shown that membrane surfaces in the form of unilamellar vesicles containing DMPS can accelerate primary nucleation by a thousandfold at pH 6.5 by increasing the local concentration of αSyn at low lipid-to-protein ratios.[12] The same study shows that when there is an excess of membrane surface, essentially all protein is bound which inhibits aggregation by depleting the fraction of soluble monomer. In a deficit of membrane surface, both the membrane-bound and soluble monomer states are populated which leads to aggregation. It was also shown that the aggregation-accelerating effect is greatly dependent on the ionic strength of the solution, where addition of 50 mM NaCl in principle nulls the catalytic effect of the anionic vesicles, highlighting the importance of electrostatic attraction between αSyn and the lipid surface.[12] Vesicles containing gangliosides has been shown to be especially potent in accelerating αSyn aggregation under mildly acidic conditions compared to other anionic lipids.[27] Gangliosides were also identified as the lipid component responsible for the accelerating effect of exosomes on αSyn aggregation.[28]

As a concluding remark regarding the interaction between aggregating αSyn and lipids, the observed effect of the presence of lipids during aggregation is highly dependent on the solution conditions such as pH, ionic strength and the lipid-to-protein ratio, which can sometimes make the literature on this subject confusing. However, the effect of lipids can often be rationalized by considering the dominant aggregation mechanism under the current solution conditions.

Properties of lipids in α-synuclein aggregates

In contrast to studies on initial αSyn binding to lipid membranes and kinetics of aggregation, some studies have focused on the effect of lipids on the properties of αSyn aggregates when the system has reached a kinetic steady-state. It was shown that DOPC vesicles with 30 mol% DOPS spontaneously co-aggregate with αSyn monomers, which causes reduced dynamics in the lipid acyl chain.[6] Notably, this co-aggregation with lipids also caused changes in the morphology of the aggregates compared to aggregates that form in the absence of lipids. This implies that lipids are present either as adsorbed layers on the fibril surface or dispersed in the fibril structure. Co-aggregation of DMPS or DLPS vesicles was also shown to cause reduced dynamics in the lipid acyl chains and headgroups, while decreasing the anisotropy of headgroup reorientation.[4] Lipids in these co-aggregates have a reduced chain-melting enthalpy, which was rationalized by the idea that lipids are less ordered when associated with αSyn then in the pure lipid phase.

An open question from the two papers described above is how lipids are organized in co-aggregates, which can have consequences for the thermodynamic and colloidal stability of aggerates. For this reason, we addressed the question of lipid organization in aggregates in paper **III**. The question on potentially selective uptake of some lipids has also been addressed in the case of GM1, where a reduction in the GM1 to DOPC ratio could be observed after co-aggregation with αSyn at mildly acidic conditions.[5] The composition of co-aggregates can have consequences for the aggregate properties and for this reason we addressed this question and the question on selective uptake using our POPC-GM3 model system in paper **I**.

NMR methods

The aim of this chapter is to describe the theoretical and practical backgrounds of the experimental NMR spectroscopy techniques used to answer the scientific questions posed in the introduction. The description is based on the textbooks of Harris,[48] Keeler[49] and Levitt[50] together with other illustrative references.

Basic NMR concepts

In this section the generation of NMR signals and spectra, together with the basics of pulse sequences, two-dimensional and quantitative NMR are described. The description of nuclear resonance is inherently quantum mechanical. However, in this section the classical vector model will be used due to its more accessible and intuitive nature. It should be noted that the vector model does not apply to coupled spins, which will be treated in the solid-state NMR section.

Nuclear spin and bulk magnetization

The origin of signals observed by NMR is based in a property called nuclear spin, which is an intrinsic form of angular momentum for elementary particles. Because of the quantization of energy, the magnitude of the total spin angular momentum S can take the values described by

$$S = \hbar\sqrt{(s(s+1))}, \tag{11}$$

where $\hbar$ is the reduced Planck's constant and s is the spin quantum number. NMR-active nuclei have $S \neq 0$ and the biological molecules investigated in the scope of this thesis were all probed via spin-1/2 nuclei (^{1}H, ^{13}C and ^{31}P). The vector model of NMR is based on the description of magnetic dipole moments as vectors. The magnetic moment $\boldsymbol{\mu}$ of a nucleus is proportional to the spin angular momentum as

$$\boldsymbol{\mu} = \gamma\mathbf{S}, \tag{12}$$

where γ is the gyromagnetic ratio of the specific nuclei. In a macroscopic sample there are typically astronomic numbers of nuclei present; in a 1 mM solution of sample in a 0.5 mL NMR tube there are $3 \cdot 10^{17}$ molecules of solute, each potentially bearing many NMR-active nuclei. The net magnetization vector is

$$\mathbf{M}_0 = \sum_i \boldsymbol{\mu}_i, \tag{13}$$

where i is the individual spin index. However, the magnetic moments of these individual nuclei do not add up to an observable macroscopic magnetization at room temperature because their directions are rapidly reoriented by thermal fluctuations. To overcome this problem the sample is inserted into a strong external magnetic field $\mathbf{B}_0$, which causes a slight, but sufficient net alignment of magnetic moments. Due to interaction with the $\mathbf{B}_0$ field, $\mathbf{M}_0$ starts to precess (Fig. 7) with a frequency ω_0 called the Larmor- or resonance frequency which leads to the fundamental equation of NMR

$$\omega_0 = \gamma B_0, \tag{14}$$

where B_0 is the magnitude of $\mathbf{B}_0$.

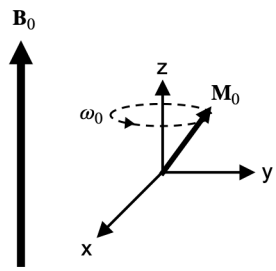

Figure 7
Prescession of the net magnetization vector $\mathbf{M}_0$ with the Larmor frequency ω_0 in an external magnetic field $\mathbf{B}_0$.

Chemical analysis by NMR is powerful because of a phenomenon known as the chemical shift that allows resolution of different chemical groups based on molecular structure. Because moving electric charges in chemical bonds generate local magnetic fields, the resonance frequency becomes a function of chemical structure and Eq. 14 becomes

$$\omega_0 = \gamma(1 - \sigma)B_0, \tag{15}$$

where σ is the shielding constant that depends on the local distribution of electrons. The chemical shift quantity δ is then defined as the resonance frequency relative to a reference compound expressed in parts per million (ppm).

The free induction decay and relaxation

At thermal equilibrium, the net magnetization $\mathbf{M}_0$ is aligned with the $\mathbf{B}_0$ field and can be probed with additional radiofrequency (RF) fields or pulses. In a paper published in 1946,[51] one of the pioneers of NMR Felix Bloch reported on the principles of nuclear induction: how RF fields $\mathbf{B}_1$ at a right angle to the $\mathbf{B}_0$ field can induce an observable voltage from a sample in an electromagnetic coil. This induced voltage became the standard detection principle of NMR signals. In the paper it was also noted that the effect was strongest at certain resonance conditions (which varies for different nuclei according to Eq. 14) and that the signal decays exponentially in time by small (in relation to $\mathbf{B}_0$ and $\mathbf{B}_1$) internuclear fields on time scales described by the relaxation times T_1 and T_2. The topic of relaxation will be treated in more detail in the section on solid-state NMR.

Because of the orientation of the coil in the laboratory coordinate system, precession of $\mathbf{M}_0$ in the x-y plane causes Faraday induction. The components of $\mathbf{M}_0$ in the x-y plane decays in time with the rate $R_2 = 1/T_2$, while $\mathbf{M}_0$ regains the equilibrium orientation along the z-axis with the rate $R_1 = 1/T_1$ in the aftermath of a $\mathbf{B}_0$ pulse. The time-domain signal can then be described as

$$S(t) = M_0 \exp(i\omega t) \exp(-t/T_2), \tag{16}$$

where M_0 is the magnitude of $\mathbf{M}_0$, i is the imaginary unit and t is time. The total (experimentally observed) signal from a sample is then the sum of signals from the spin ensemble described by Eq. 16, with a distribution of amplitudes, frequencies, and relaxation rates related to the sample composition, molecular structure, and dynamics respectively. To present the NMR signal in a way that is readily interpretable by humans, the time-domain signal is Fourier transformed to produce a spectrum

$$S(\omega) = \sum_{i=1}^{N} S(t_i) \cos(2\pi\omega t_i), \tag{17}$$

where N is the total number of discrete points in the FID, ω is the frequency and t_i is point number i in the time-domain signal. Just like how our ears translate acoustic waves in the air around us into sounds with distinguishable frequencies, the Fourier transformed FID produces a spectrum containing spectral lines with characteristic amplitudes, chemical shifts (frequencies) and widths (relaxation rates). The process of generating a FID and Fourier transformation is illustrated in Fig 8.

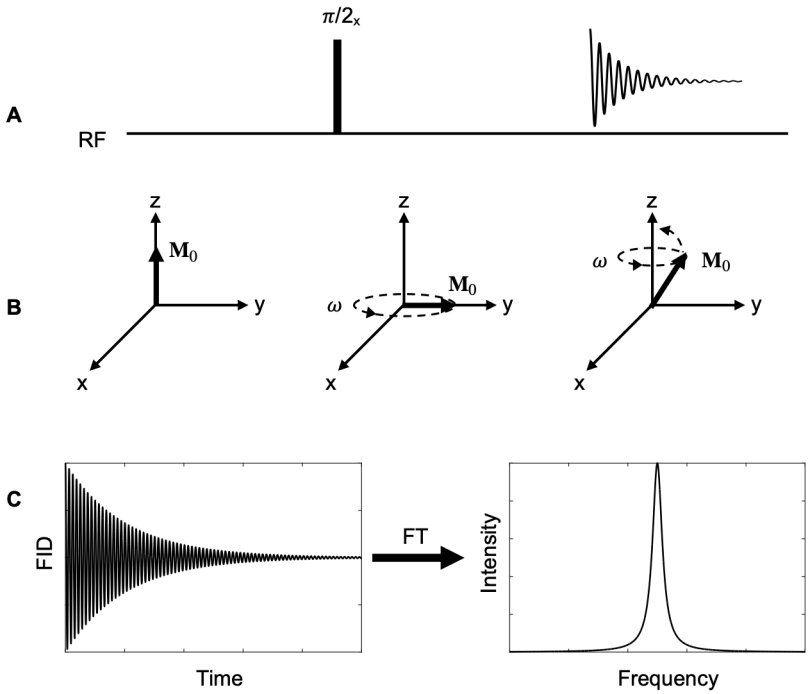

Figure 8
Generation of a free induction decay (FID) and Fourier transformation. (**A**) The pulse sequence for the pulse-acquire experiment consists of a single pulse, acqusition period and recycle delay. (**B**) Effects on the net magnetization vector $\mathbf{M}_0$. Immediately after the $\pi/2_x$ pulse, $\mathbf{M}_0$ lies in the transverse (x-y) plane where precession at the frequency ω induces an electric current in the coil. The orientation of $\mathbf{M}_0$ gradually aligns back with the equilibrium direction parallel to the z-axis of the laboratory frame due to longitudinal relaxation with the time constant T_1. (**C**) The shape of the free induction decay (FID) described by Eq. 16. Fourier transformation (FT) of the FID yields the NMR spectrum.

The application of Fourier transform NMR was introduced by Richard Ernst and co-workers in 1966.[52] Before that introduction, the $\mathbf{B}_1$ field was "swept" to excite a single resonance condition at a time to record a spectrum instead of exciting a range of nuclei with slightly different Larmor frequencies at once using a $\mathbf{B}_1$ pulse and recording a FID. Because the information content of the Fourier transformed FID is equivalent to the spectrum, an obvious advantage of the pulsed technique is that no time was lost scanning only baseline. This led to 10-fold improvements in signal-to-noise ratios per unit time when consecutive FIDs are co-added before Fourier transformation. The not-as-obvious but revolutionary implications were the enabling of pulse sequences and multidimensional experiments.

Pulse sequences have two basic building blocks: pulses (RF irradiation) and delays (waiting times). The pulse sequence for a basic 1D pulse-acquire experiment is shown in Fig. 8A. When $\mathbf{M}_0$ is at thermal equilibrium in the $\mathbf{B}_0$ field, the sample can be excited by a pulse that has been calibrated to rotate $\mathbf{M}_0$ into the x-y plane to produce a FID (Fig. 8B). The FID contains molecular information as described by

Eq. 16 and can be Fourier transformed into a spectrum (Fig. 8C). A delay time follows next where the net magnetization returns to the ground state before the next pulse is applied.

Pulse sequences and multidimensional experiments

The power of pulse sequences comes from the possibility to tailor the information content of the FID by preparing the spin system in a state that is sensitive to the interactions of interest. More advanced applications will be introduced in the section on solid-state NMR, for now a basic example will be the spin-echo sequence (Fig. 9). The effect of a spin echo is to refocus the precession offset which allows the magnetization to be manipulated independently of chemical shifts and can illustrate how a pulse sequence selects for information content. Because the system is prepared in a state that is sensitive to T_2 relaxation (the excitation pulse created transverse magnetization that relaxes in time according to Eq. 16), the length of the delay time τ can control how much the signal is weighted by this effect. When the chemical shift evolution and $\mathbf{B}_0$ inhomogeneities are "filtered out" by the π-pulse, the signal attenuation can be used to estimate T_2 in Eq. 16 by measuring the signal as a function of τ.

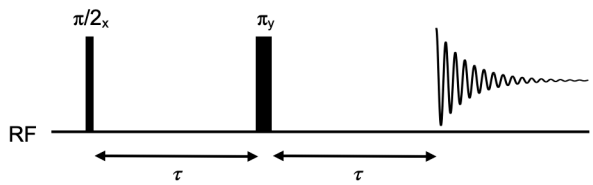

Figure 9
The spin echo pulse sequence. The first $\pi/2_x$ pulse brings $\mathbf{M}_0$ into the x-y plane where coherence is lost during the delay τ when the individual magnetic moments precess with different frequencies based on their chemical shifts. The π_y pulse effectively mirrors the phases acquired by the individual spins, which align in phase after another equally long delay τ when the direction of precession has been reversed by the π_y pulse. The resulting signal is an "echo" where the chemical shift offset has been refocused.

NMR spectroscopy is known for routine usage of multidimensional and correlation experiments. A schematic 2D experiment is shown in Fig. 10, and contains four essential periods: preparation, evolution, mixing and detection. During preparation the spin system is manipulated using pulses and delays into a state that is sensitive to the interaction of interest. During the evolution period the system evolves under that interaction over an increment in the time dimension t_1, which consequently encodes the signal with information. In the mixing period an observable signal is prepared and then recording during the detection period t_2. By varying the length of the time t_1 systematically, the interaction can be correlated with information in the t_2 dimension (typically the chemical shift). This procedure yields correlation cross-

peaks in the Fourier transformed 2D spectrum, which for example can be related to the covalent structure or distance between nuclei in space using the COSY[53] and NOESY[54] experiments respectively. This lays the foundation for 3D-structure determination of proteins using NMR, where a large set of molecular constraints can be fitted to produce a structure.[55]

In this thesis work a 2D pulse sequence[56] was applied in an attempt to measure interatomic distances between lipids and αSyn by exploiting spin-diffusion in the solid-state to correlate ^{1}H and ^{13}C chemical shifts. This method is described in more detail in the section on solid-state NMR of lipids.

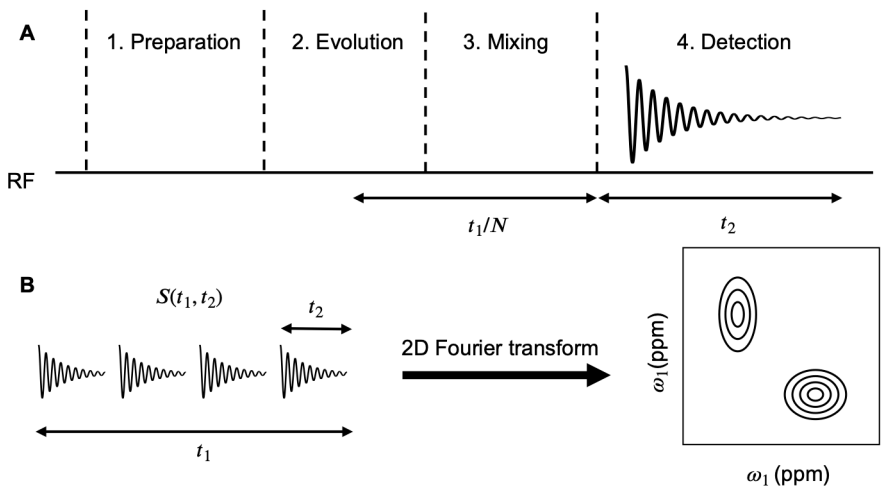

Figure 10
Schematic 2D NMR experiment. (**A**) During the preparation period the spin system is brought to a state that is sensitive to the interaction of interest. During the evolution period the signal is encoded with information by varing the increment t_1/N in the indirect dimension. During the mixing period an observable signal is prepared followed by a detection period where a FID is recorded for each increment in t_1 (**B**) Fourier transformation in both time variables yields a 2D spectrum commonly plotted as a contour. In correlation experiments cross-peaks indicate coupled spins that can be resolved by their chemical shifts (depending on the experiment type).

Quantitative NMR

The NMR signal is directly proportional to the number of nuclei with a given resonance frequency, which makes NMR a useful tool for quantitative analysis.[57] Some important pre-conditions for quantitative NMR are high signal-to-noise, analyte solubility, no peak overlap, proper shimming, pulse calibration and a long enough recycle delay for the magnetization to reach its equilibrium value along the z-axis after each scan. After acquisition the spectrum is phase- and baseline corrected and the peak of interest is integrated and normalised by number of nuclei for comparison on a mol-per-mol basis. The relative proportion of two molecular species A and B is then

$$\frac{n_A}{n_B} = \frac{I_A}{I_B}\frac{N_B}{N_A}, \tag{18}$$

where n is the molar amount, I is the integrated area and N is the number of nuclei. Absolute amounts of analyte can be determined from external calibration or by the addition of a known amount of internal standard. In paper **I** the absolute amount of lipids was measured in samples extracted from the supernatant of mixtures with lipid vesicles and αSyn using tetramethyl silane (TMS) in chloroform/methanol as an internal standard. When the concentration of an internal standard (IS) is known, the concentration of analyte A can be determined as

$$C_A = C_{IS}\frac{I_A}{N_A}/\frac{I_{IS}}{N_{IS}}. \tag{19}$$

Solid-state NMR

Solid-state NMR is a powerful tool that can provide unique information on dynamics and structure of solid- or semi-solid materials like liquid crystals. Because the materials of interest in this thesis (fibrillar protein, self-assembled lipids) are highly anisotropic with strong spin-spin couplings and short T_2-times, measurements without solid-state NMR techniques such as magic-angle spinning (MAS) and heteronuclear decoupling would yield featureless spectra with low resolution and intensity. This section will describe the essentials of the solid-state NMR techniques that were routinely used during the thesis work.

The following subsections will contain some descriptions of the most important NMR interactions that are the basis for the results in the thesis work. Interactions in NMR are typically described using Hamiltonian theory, where the Hamilton operator $\hat{\mathcal{H}}$ obtains the energy of a spin state by operating on the spin wavefunction. This energy determines the positions of energy levels in an energy level diagram which is commonly used to illustrate spectroscopic transitions (the analogue for energy level differences in NMR is the resonance frequency). The full Hamiltonian for the spin magnetic interactions can be written as

$$\hat{\mathcal{H}}_{\text{spin magnetic}} = \hat{\mathcal{H}}_{\text{static}} + \hat{\mathcal{H}}_{\text{RF}} + \hat{\mathcal{H}}_{\text{CS}} + \hat{\mathcal{H}}_{\text{DD}} + \hat{\mathcal{H}}_{\text{J}} + \hat{\mathcal{H}}_{\text{Q}} \tag{20}$$

where the interactions are represented by $\hat{\mathcal{H}}_{\text{static}}$ between a spin and the static external $\mathbf{B}_0$ field, $\hat{\mathcal{H}}_{\text{RF}}$ between the spin and RF pulses, $\hat{\mathcal{H}}_{\text{CS}}$ for the chemical shift, $\hat{\mathcal{H}}_{\text{DD}}$ for dipole-dipole coupling, $\hat{\mathcal{H}}_{\text{J}}$ for J-coupling and $\hat{\mathcal{H}}_{\text{Q}}$ for quadrupolar coupling. The form of these terms is further subject to certain simplifications such as the secular approximation and motional averaging, where the latter depends on the physical state of the sample.

Anisotropic interactions

Before discussing any specific solid-state NMR techniques, it is useful to introduce the concept of anisotropic interactions. Anisotropic properties vary with orientation, whereas isotropic properties do not. A simple example is that the shape of an isotropic object like a sphere does not depend on what direction we view it from, it looks like a sphere from all directions and can be defined with a single parameter, the radius. In contrast, the shape of an anisotropic object like an ellipsoid will vary depending on if we view it from the top or from the side and is defined by its semi-axes. In a similar way, how the nuclear spin and magnetic fields interact (see each other) can also depend on their relative orientation.

The terms in Eq. 20 can be organized into external and internal terms, where the internal terms $\hat{\mathcal{H}}_{\mathrm{CS}}$, $\hat{\mathcal{H}}_{\mathrm{DD}}$, $\hat{\mathcal{H}}_{\mathrm{J}}$ and $\hat{\mathcal{H}}_{\mathrm{Q}}$ describes interactions within the sample itself and carry information on molecular structure and dynamics. These interactions are in general anisotropic as they depend on the orientation relative to the external $\mathbf{B}_0$ field. For spin-1/2 nuclei like ^{1}H, ^{13}C and ^{31}P, which do not possess and quadrupolar moment, the main interactions of interest for the thesis work are the chemical shift and dipolar terms.

An essential difference between solution- and solid-state NMR is rapid tumbling in random directions of molecules in the former. For analogy with the paragraphs above, imagine that you are observing a cylinder from the side. It clearly has different length and width, but if it is rotated rapidly in random directions it will appear as a blurry sphere (it appears isotropic). This typically leads to partial or complete averaging of anisotropic interactions which are scaled by the second-order Legendre polynomial $(3\cos^2\theta - 1)/2$, where θ is the angle between the principal axis of the interaction and $\mathbf{B}_0$. This is described mathematically by the isotropic average of the orientation dependence

$$\left\langle \frac{3\cos^2\theta - 1}{2} \right\rangle = \frac{1}{\pi} \int_0^{\pi} p(\theta) \frac{(3\cos^2\theta - 1)}{2} \mathrm{d}\theta. \qquad (21)$$

Note the form of the left-hand side of Eq. 21, which is equal to the definition of the order parameter $|S_{\mathrm{CH}}|$ in Eq. 10. The second order Legendre polynomial appears frequently in the description of anisotropic interactions in NMR because it describes the geometrically simplest deformation of a circle and is thus a measure of anisotropy. The angle-specific weights $p(\theta) = \sin\theta$ in Eq. 21 because the angle perpendicular to $\mathbf{B}_0$ is most probable, corresponding to the population of angles along the equator of a sphere centered on the origin of the laboratory coordinate system. In this case Eq. 21 equals zero, and anisotropic terms vanish in solution NMR. In contrast, there are typically strong correlations between nuclear positions and molecular orientations together with slow dynamics in the solid state, which means that anisotropic interactions will have a large effect on solid-state NMR spectra.

Chemical shift anisotropy

The chemical shift is generally anisotropic which can be exploited to extract valuable information. Anisotropic interactions in NMR are described using rank 2 tensors and can be visualized as ellipsoids where the directions and lengths of the semiaxes are defined by the respective eigenvectors and eigenvalues. Depending on the molecular geometry and electron distribution, the shielding will vary in the x, y and z-dimensions which is described by the chemical shift tensor

$$\boldsymbol{\delta} = \begin{pmatrix} \delta_{xx} & \delta_{xy} & \delta_{xz} \\ \delta_{yx} & \delta_{yy} & \delta_{yz} \\ \delta_{zx} & \delta_{zy} & \delta_{zz} \end{pmatrix}, \tag{22}$$

where the elements δ_{ii} describe the chemical shift in the combinations of x,y and z directions and is symmetric in the off-diagonal elements ($\delta_{yx} = \delta_{xy}$ etc.). The effective field at a nucleus is then

$$\mathbf{B}_{eff} = \boldsymbol{\delta}\mathbf{B}_0 \tag{23}$$

and the chemical shift Hamiltonian is equal to

$$\hat{\mathscr{H}}_{CS} = \sum_j (-\gamma \hat{\mathbf{I}}_j \mathbf{B}_{eff}), \tag{24}$$

where $\hat{\mathbf{I}}_j$ is the spin angular momentum operator associated with spin j. In the secular approximation only the zz-term is retained and after motional averaging in an anisotropic liquid Eq. 24 becomes

$$\hat{\mathscr{H}}_{CS} = \sum_j (-\gamma B_0 \left(1 + \int p(\theta)\, \delta^j_{zz}(\theta)\, d\theta\right) \hat{I}_{jz}, \tag{25}$$

where $p(\theta)$ is a probability distribution of possible orientations. A direct manifestation of chemical shift anisotropy (CSA) is that if a sample is macroscopically oriented (for example on a glass slide), the frequency of the spectral lines depends on the tilt angle between the sample and $\mathbf{B}_0$. In a non-crystalline solid the so-called powder spectrum contains a superposition of many domains with a statistical distribution of orientations, giving rise to broad spectral peaks that contain information on how lipids are arranged, which will be described further in the section on ^{31}P NMR of lipids.

Dipolar coupling

The dipolar interaction is analogous to the forces that bar magnets exert on each other. It is of value in structural studies of anisotropic materials due to the distance and angular dependence which is independent of long-range order that is required for analysis by other physical techniques such as X-ray scattering. The heteronuclear dipolar coupling Hamiltonian in an anisotropic liquid can be written as

$$\hat{\mathscr{H}}_{\mathrm{DD}} = \sum_{\mathrm{j}} \sum_{\mathrm{k}} d_{\mathrm{jk}} \hat{I}_{\mathrm{jz}} \hat{I}_{\mathrm{kz}} p\left(\theta_{\mathrm{jk}}\right) (3\cos^2\theta_{\mathrm{jk}} - 1), \tag{26}$$

where θ_{jk} is the angle between the internuclear vector and $\mathbf{B}_0$ and d_{jk} is equal to

$$d_{\mathrm{jk}} = b_{\mathrm{jk}} \frac{1}{2N} \sum_{\theta_{\mathrm{jk}}} p(\theta_{\mathrm{jk}})(3\cos^2\theta_{\mathrm{jk}} - 1), \tag{27}$$

where N is the total number of dipolar coupling pairs. The dipolar coupling constant is defined as

$$b_{\mathrm{jk}} = -\frac{\mu_0}{4\pi} \frac{\gamma_{\mathrm{j}} \gamma_{\mathrm{k}} \hbar}{r_{\mathrm{jk}}^3}, \tag{28}$$

where the magnetic constant is $\mu_0 = 4\pi \times 10^{-7}\mathrm{H\ m^{-1}}$ and r_{jk}^3 is the cube of the internuclear distance. The geometric parameters involved in dipole-dipole coupling are illustrated in Fig. 11.

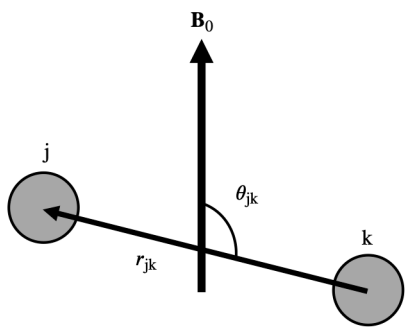

Figure 11
Dipole-dipole coupling between two nuclear spins j and k. The energy associated with the coupling depends on the internuclear distance as r_{jk}^{-3} and the angle θ_{jk} between the internuclear vector and the external magnetic field $\mathbf{B}_0$.

From Eq. 28 a strong distance dependence is evident, which implies that typically only the dipolar fields of the closest nuclei in space interact strongly with each other. In practice however, large dipolar coupling networks are present in organic molecules between ^{1}H spins which significantly complicates spectra in the absence

of resolution enhancement techniques like MAS, which is described more in the next section.

The value of b_{jk} can be obtained directly from dipolar peak splittings in spectra of isolated spin pairs in crystals called Pake patterns, however, in more heterogeneous systems such as liquid crystals, other methods are needed to measure the dipolar coupling because of the presence of large shielding anisotropies and the necessity for MAS to improve the sensitivity and resolution, which obscures and weakens the dipolar splittings as described in the following section on MAS. In response to these problems methods based on dipolar recoupling under MAS were developed,[58] which are incorporated in more modern separated local field (SLF)[59] type experiments such as R-PDLF.[60]

Magic-angle spinning

MAS is a technique used to improve the spectral resolution in solid-state NMR. The information density of solid-state NMR spectra originating from CSA and dipolar coupling has a downside; peaks are broadened and resolution is lost, which makes analysis of a complex sample difficult. MAS improves the spectral resolution by modifying the anisotropic geometric factor in Eq. 27. This is done by rotating the sample in a cylindrical rotor with a frequency ω_r, which simulates the averaging that occurs naturally in liquids. This motional averaging can be described with

$$\langle 3\cos^2\theta - 1\rangle = \tfrac{1}{2}(3\cos^2\beta - 1)(3\cos^2\chi - 1), \qquad (29)$$

where θ, β and χ are the angles between the dipolar vector $\mathbf{r}$ and $\mathbf{B}_0$, between the rotation axis and $\mathbf{B}_0$ and between the dipolar vector and the rotation axis respectively (Fig. 12).

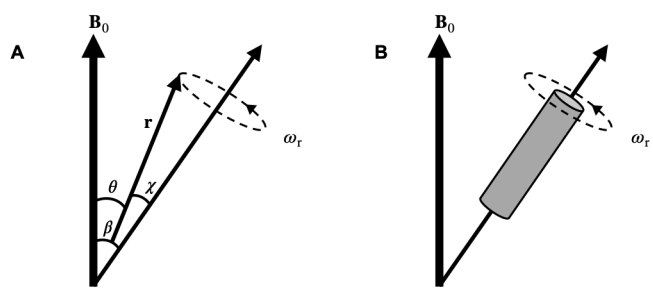

Figure 12
Magic-angle spinning in solid-state NMR. (**A**) Geometry of sample spinning about the magic angle. The sample is oriented along the rotation axis which is mechanically set to the angle $\beta = 54.7°$ (magic angle) to the external magnetic field $\mathbf{B}_0$ and spinning with the frequency ω_r. The dipolar vector $\mathbf{r}$ representing two dipolar coupled spins in the sample is oriented at the angle χ with the rotation axis, which depends on the position of the molecules in the sample. When

the sample is oriented at the magic angle, the anisotropic scaling factor for dipolar interactions is equal to zero. (**B**) Illustration of a rotor (cylindrical sample holder) rotating at the magic angle.

In the case of an unoriented sample, the values of χ will have a powder distribution but it is still possible to physically orient the sample at the angle $\beta = 54.7°$ which will scale Eq. 29 to zero, which leads to narrower lines and better resolution. The rotation rate affects the effectiveness of the averaging and for near complete averaging ω_r needs to be the same or greater than the interaction strength of the broadening mechanism (in this case dipolar coupling). If ω_r is not fast enough, spinning sidebands will appear in the spectrum separated by multiples of ω_r, which can also be exploited for information on the CSA.[61] The analogy with motional averaging in liquids and MAS becomes even more apparent when considering the more recent introduction of MAS spheres.[62]

Decoupling and recoupling

Decoupling refers to the techniques where RF irradiation is used to lessen the effect of spin-spin couplings. Because of the abundance of ^{1}H in the environment of ^{13}C nuclei in organic molecules, decoupling of the ^{1}H-^{13}C dipolar interaction is crucial for obtaining high-resolution solid-state ^{13}C spectra. Typically, the ^{1}H-^{13}C heteronuclear dipolar coupling is removed by high-power broadband irradiation on the ^{1}H channel. The conventional two pulse phase modulation (TPPM) decoupling sequence[63] applies a train of pulses alternating between two phases on the ^{1}H channel to achieve decoupling and was used for all experiments in paper **I**. In papers **II** and **III** SPINAL-64[64] decoupling was used, which is more efficient than TPPM for liquid crystals.

Detection on the ^{1}H channel is usually avoided in for organic molecules in solid-state NMR due to the abundance of protons and strong ^{1}H-^{1}H dipolar coupling which leads to low resolution. This problem can be partially remedied by high MAS frequencies over 100 kHz.[65] Instruments with such fast MAS is currently not widely available, but instead homonuclear decoupling sequences such as eDUMBO[66] which uses high-power irradiation on the ^{1}H channel together with an intricate phase cycling scheme can be used. For the work in paper **IV** the eDUMBO decoupling sequence was used to improve the resolution of the ^{1}H dimension in HETCOR spectra of lipids in αSyn aggregates acquired under conditions suitable for dynamic nuclear polarization (DNP).

Recoupling refers to the selective reintroduction of spin-spin interactions, for example during the mixing period of a 2D experiment to encode information. Recoupling schemes are complicated by the necessity of simultaneous use of MAS. The R-type proton detected local field (R-PDLF)[67] 2D experiment can be used to measure dipolar splittings in unlabeled materials under MAS and reintroduces the heteronuclear ^{1}H-^{13}C dipolar coupling by rotor synchronized pulses while refocusing the ^{13}C CSA. Because the dipolar coupling is probed on the ^{1}H channel,

there is typically high resolution in the dipolar dimension after polarization transfer and detection on the ^{13}C channel. The R-PDLF experiment was used in the work on papers **II** and **III** and is described more in the section on solid-state NMR of lipids.

Cross-polarization

Cross-polarization (CP)[68] is a pulse sequence used to enhance the signal from isotopically dilute and low-γ nuclei by exploiting the strong ^{1}H-^{13}C dipole coupling in anisotropic materials. The principle of CP is that dipolar coupling-mediated magnetization transfer from ^{1}H to ^{13}C is allowed when the two spin populations are precessing with the same frequency in the x-y plane. This condition is called the Hartman-Hahn condition

$$\gamma_{\mathrm{I}} B_{1,\mathrm{I}} = \gamma_{\mathrm{S}} B_{1,\mathrm{S}}, \tag{30}$$

where γ_{i} is the gyromagnetic ratio of the abundant (I) and dilute (S) spins and B_1 are precisely calibrated RF pulses. In the pulse sequence for CP (Fig. 13) polarization is transferred during the contact time τ_{CP}.

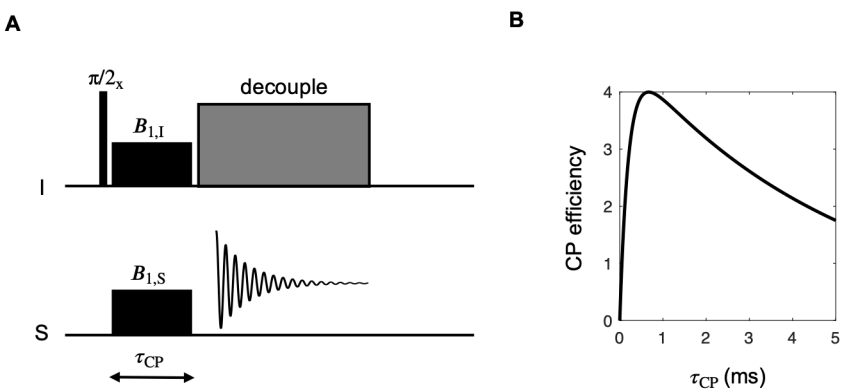

Figure 13
Cross-polarization (CP). (**A**) Pulse sequence for CP. Transverse magnetization is created from the abundant spins I, which is subsequently spin-locked and made to precess at the Hartman-Hahn condition together with the dilute spins S. During the CP contact time τ_{CP} polarization transfer occurs, followed by decoupling while the FID is recorded on the S channel where the signal has been enhanced by up to the factor $\gamma_{\mathrm{I}}/\gamma_{\mathrm{S}}$. (**B**) CP efficiency as a function of τ_{CP} (Eq. 32). There is a well-defined maximum in the signal enhancement which is limited by the rate of polarization transfer and decay of the ^{1}H spin reservoir from relaxation respectively.

The mechanism for CP is commonly explained by a thermodynamic spin temperature argument, where a high-heat capacity ^{1}H reservoir at low spin temperature is in contact with a low-heat capacity ^{13}C reservoir at practically infinite spin temperature. During the Hartman-Hahn match the two reservoirs are in thermal

contact and there occurs an equalization of spin heat which gives a ^{13}C polarization equal to

$$M_C = \frac{1}{4}\gamma_C^2\hbar^2 N_C \frac{\gamma_H}{\gamma_C} B_0/kT_L, \quad (31)$$

where N_C is the number of ^{13}C spins, k is a constant and T_L is the lattice temperature. This corresponds to a signal enhancement by the ratio γ_I/γ_S, which for ^1H and ^{13}C is around a factor four. The CP intensity is described by

$$\frac{I_{CP}}{I_{DP}^{eq}} = \frac{\gamma_H}{\gamma_C}\frac{\exp(-R_{1\rho}^H\tau_{CP})-\exp(-R_{CH}\tau_{CP})}{1-R_{1\rho}^H/R_{CH}}, \quad (32)$$

where I_{CP} is the CP intensity, I_{DP}^{eq} is the intensity from a standard pulse-acquire experiment, $R_{1\rho}^H$ is the relaxation rate constant for ^1H in the rotating frame, τ_{CP} is the contact time and R_{CH} is the rate of polarization transfer. Because the dipole interaction is averaged out by fast motions in liquids, CP is a solid-state NMR technique. However, the INEPT[69] sequence for liquids depends on *J*-coupling and can used to together with CP as a mobility filter for studies on anisotropic liquids. The use of CP and INEPT for this purpose will be described more in the following section.

Solid-state NMR of lipid membranes

This section aims to outline the specific solid-state NMR techniques that were used to perform the experiments on structure and dynamics of lipids and lipids in amyloid aggregates during the thesis work.

CP and INEPT intensities

For self-assembled lipid phases, both CP and INEPT can be effective for signal enhancement and be used to gain qualitative information on the dynamics. The dependence of the CP intensity on dynamics comes from the factors $R_{1\rho}^H$ and R_{CH} in Eq. 32, which can be expressed using the random fields model[48] as

$$R_{1\rho}^H = \gamma_H^2 b_H^2 \frac{1}{2}\left[j(\omega_1^H) + j(\omega_0^H)\right] \quad (33)$$

and

$$R_{CH} = \gamma_C^2 b_C^2 \frac{1}{2} j(\omega_1^H - \omega_1^C), \tag{34}$$

where $b_{H/C}^2$ is the root-mean-square amplitude of the fluctuating magnetic field, j is the spectral density function at the proton spin-lock frequency ω_1^H and Larmor frequency $\omega_0^{H/C}$ respectively. The spectral density is the Fourier transform of $g(\tau)$, and is used to samples the available motional intensity for driving relaxation in these cases. The spectral density will be described more in the section on model-free formalism. The INEPT intensity can be described as

$$\frac{I_{INEPT}}{I_{DP}^{eq}} = \frac{\sqrt{2}}{4}\frac{\gamma_H}{\gamma_C}\exp(-\frac{R_2^H}{2J_{CH}} - \frac{R_2^C}{8J_{CH}}), \tag{35}$$

where J_{CH} is the C-H scalar coupling constant and $R_2^{C/H}$ are transverse relaxation constants when using the optimized time delays $\tau_1 = J_{CH}^{-1}/4$ and $\tau_2 = J_{CH}^{-1}/8$. From these expressions, CP and INEPT are clearly dynamic filters based on $R_{1\rho}^H$ and R_{CH} rates for CP and $R_2^{C/H}$ for INEPT. Solid-like materials with slow dynamics and strong dipole coupling typically have high R_{CH} and R_2-rates, which enhances CP and limits INEPT enhancement. A straightforward application for this is resolving lipid segments and protein residues in mixed aggregates in paper **I**.

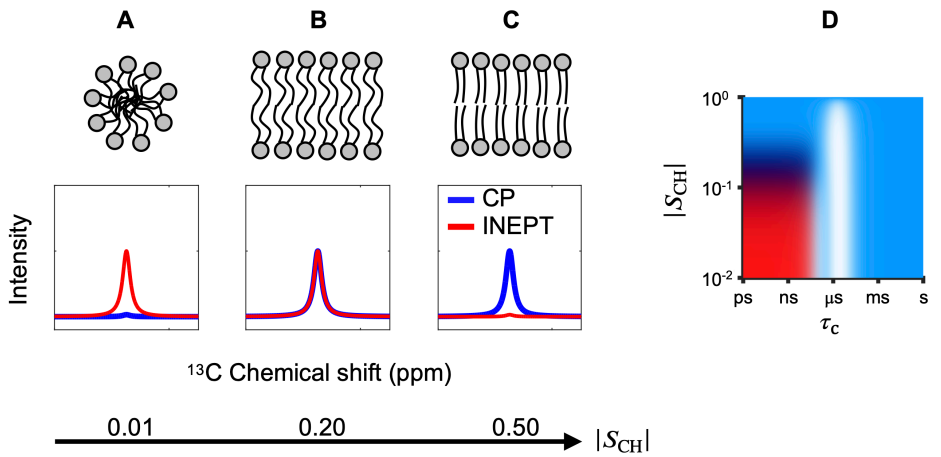

Figure 14
Relative CP and INEPT intensities for investigating the dynamics of lipids. (**A**) Rapid, isotropic reorientation such as in micelles leads to $I_{INEPT} \gg I_{CP} \approx 0$. (**B**) Rapid, anisotropic reorientation in a liquid crystalline phase leads to $I_{INEPT} \approx I_{CP}$. (**C**) Slow, or highly anisotropic reorientation leads to $I_{CP} \gg I_{INEPT} \approx 0$. (**D**) Changes in the relative CP and INEPT intensities can be caused by changes in either or both the parameters $|S_{CH}|$ and τ_c. The blue regions give intense CP while the red region gives intense INEPT. The white regions gives no INEPT or CP due to interference from MAS. Reproduced from Nowacka et al. [70]

The relative intensities of CP and INEPT can be used to qualitatively describe lipid dynamics based on the C-H order parameter $|S_{CH}|$ and correlation time τ_c in the model of Nowacka.[70] Comparing the relative CP to INEPT intensities are useful to rapidly screen the lipid dynamics under different conditions (Fig. 14), however a limitation of the CP and INEPT approach to study dynamics is that changes in $|S_{CH}|$ and τ_e are confounded (Fig. 14D).

Separated local field experiments

Separated local field experiments induce a local field during a period of an NMR experiment, for example by recoupling dipolar couplings under MAS during the evolution time of a 2D experiment. The recoupling encodes information on the dipolar interaction in an R-type proton detected separate local field (R-PDLF)[67] experiment (Fig. 15A). This type of experiment yields dipolar splittings $\Delta\nu^{R-PDLF}$ in the indirect dimension, which are proportional to the order parameter $|S_{CH}|$ as expressed by

$$\Delta\nu^{R-PDLF} = 0.315 d_{CH}|S_{CH}|, \qquad (36)$$

where d_{CH} is the C-H dipolar coupling constant, approximated to 21.5 kHz.[71] Many studies in the past have used deuteration methods to exchange ^{1}H for ^{2}H in molecules to be able to measure order parameters $|S_{CD}|$ from quadrupolar splittings,[72] however using recoupling methods like R-PDLF it is possible to obtain $|S_{CH}|$ at natural isotopic abundance. Because protons only communicate with relatively few ^{13}C spins at natural isotopic abundance (1.1% for ^{13}C), another advantage of the R-PDLF method is that it offers very high resolution in the indirect dimension as the dipolar field is probed on the ^{1}H channel where the spin dynamics are dominated by two-spin interactions. Each $R18_1^7$ recoupling block contains a π_x-pulse pair with reverse phases, which is repeated 9 times each rotor period. Based on symmetry principles this imposes certain selection rules on the components of the recoupled first-order average Hamiltonian, which can recouple CSA, dipolar coupling or J-couplings.[73]

Fig. 15B shows a 2D R-PDLF spectrum obtained on the POPC-GM3 system at 310 K from paper **III**. Dynamic filtering using CP and INEPT adds an additional way to resolve resonances, which combined with the high resolution in the dipolar dimension offered by the R-PDLF experiment allows assignment of dipolar splittings and calculation of $|S_{CH}|$.

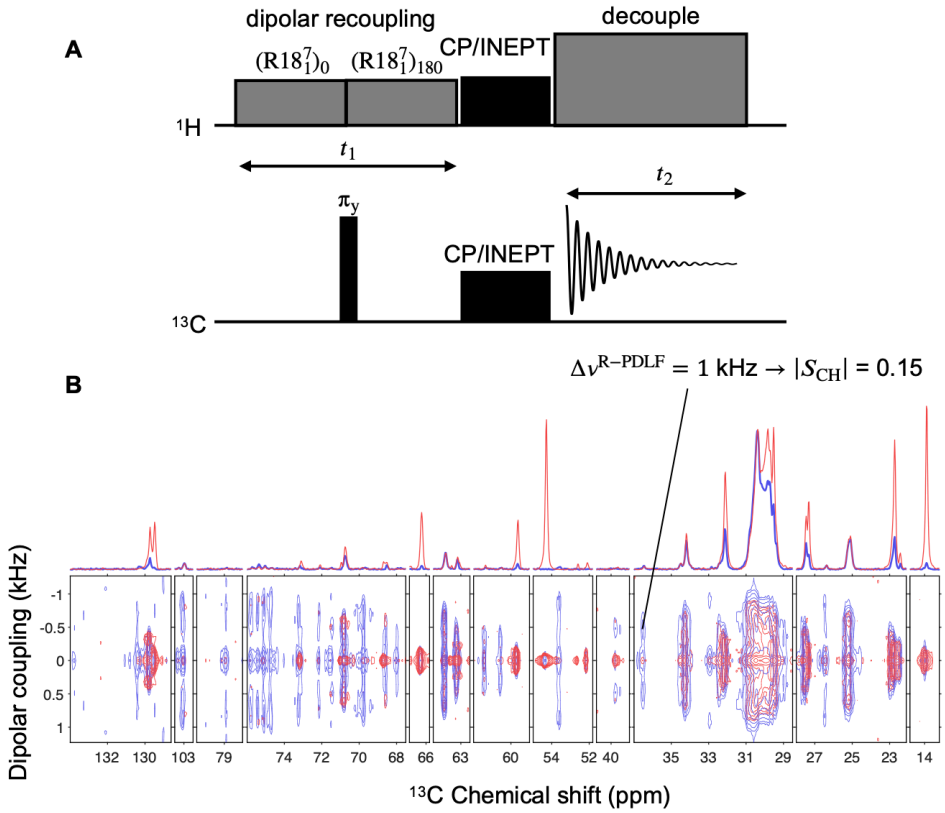

Figure 15
The 2D R-PDLF experiment. (**A**) Pulse sequence for 2D R-PDLF. During the t_1-delay, recoupling of the ^{1}H-^{13}C dipolar coupling is achived by a series of rotor-synchronized π-pulses by the $(R18_1^7)_0$ and $(R18_1^7)_{180}$ blocks. During the same period the CSA is refocused on the ^{13}C channel by a π_y-pulse. By probing the dipolar field on the ^{1}H channel, the system is dominated by two-spin interactions as ^{13}C is isotopically dilute at natural isotopic abundance, which leads to high resolution in the dipolar dimension. The dipolar modulated polarization is then transferred for detection on the ^{13}C channel by CP or INEPT where the FID is recorded. A 2D spectrum is obtained by Fourier transformation in t_1 and t_2. (**B**) Example 2D R-PDLF data from paper **III** on an equilibrum phase of POPC with 30 mol% GM3 obtained at a ^{13}C Larmor frequency of 125 MHz with 5 kHz MAS and CP (blue) and INEPT (red) for polarization transfer at 310 K. The splittings in the dipolar dimension are proportional to the ^{1}H-^{13}C order parameter $|S_{CH}|$ via Eq. 36.

^{13}C Relaxation experiments

This section will describe the techniques for measuring R_1 and $R_{1\rho}$ relaxation rate constants that was used to obtain effective correlation times τ_e of lipids and α-synuclein in papers **II** and **III**. The R_1 and $R_{1\rho}$ relaxation rates are connected to the autocorrelation function $g(\tau)$ and the underlying molecular motions via the spectral density $j(\omega)$, which is the Fourier transform of $g(\tau)$. The dependence of the relaxation rates on $j(\omega)$ and molecular motions will be described in more detail in the section on model-free analysis.

Values of longitudinal relaxation constants R_1 can be measured using an inversion recovery (IR) experiment. Longitudinal magnetization is not directly observable because the FID is generated from the x- and y-components of the net magnetization. Therefore, to measure R_1, a π_x pulse is first used to displace the magnetization from the z-axis to the -z axis. This displacement is achieved in Fig. 16A by the combination of a preceding CP or INEPT block followed by a $\pi/2_x$ pulse. The magnetization vector then starts to return to the equilibrium direction aligned with the z-axis during a variable delay time t_1, which consequently encodes the signal for R_1 relaxation. A second $\pi/2_x$ read pulse allows the observation of the momentary value of the R_1-weighted signal which is described by

$$S(t_1) = S_0(1 - 2\mathrm{e}^{-t_1 R_1}). \tag{37}$$

Using the T_1-CP method by Torchia (Fig. 16A) achieves suppression of some artefacts[74] and gives the value of R_1 from the expression

$$S(t_1) = S_0 \exp(-t_1 R_{1/1\rho}), \tag{38}$$

where S_0 is the initial signal amplitude. This type of experiment with a variable delay time like in 2D NMR, but where the data is not 2D Fourier transformed is sometimes called a pseudo-2D experiment. While in principle R_1 values for all peaks in the chemical shift spectrum can be determined simultaneously using this experiment, peak overlap in a complex spectrum can pose a significant limitation.

Another type of experiment can be used to measure relaxation in the presence of a spin-lock pulse which is also referred to as relaxation in the rotating frame or $R_{1\rho}$ relaxation. This type of relaxation is reminiscent of R_1 relaxation, but instead of re-aligning with the $\mathbf{B}_0$ field, the magnetization is forced to remain in the transverse plane by applying a RF pulse (spin-locking). The magnetization then decays to a value recorded in the FID at the end of the spin-lock pulse. This process is characterized by the $R_{1\rho}$ relaxation constant and can be used to probe intermediate-fast dynamics on frequencies of 10^4-10^3 Hz at contemporary $\mathbf{B}_1$ fields. The pulse sequence for a $R_{1\rho}$ experiment is shown in Fig. 16B. Transverse magnetization is created and "locked" in the x-y plane by a $\pi/2$ phase shifted pulse and then decays with the exponential rate constant $R_{1\rho}$. Varying the duration of the spin-lock pulse encodes for $R_{1\rho}$ which is then extracted by fitting the signal to Eq. 38. Fig. 16C and 16D illustrates how R_1 and $R_{1\rho}$ values are sensitive to differences in dynamics in different molecular segments of lipids.

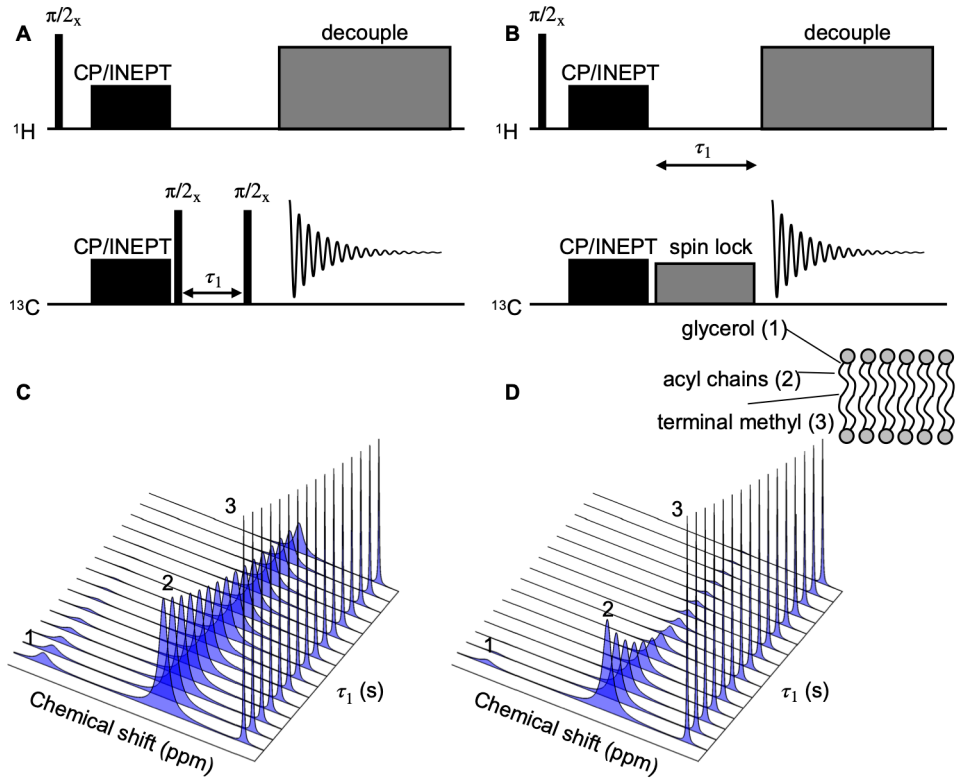

Figure 16
Measurements of R_1 and $R_{1\rho}$ relaxation rate constants. (**A**) Pulse sequence for measurement of R_1. During a sufficiently long increment in τ_1 the signal is attenuated by R_1 relaxation (Eq. 38), which is recorded as a FID after a $\pi/2_x$ read pulse. (**B**) Pulse sequence for measurement of $R_{1\rho}$. In contrast to the R_1 pulse sequence, a spin-lock pulse is applied during τ_1 which encodes for $R_{1\rho}$ in the signal attenuation. (**C**) Schematic view of the signal attenuation in the frequency domain for different lipid segments due to R_1 relaxation. Relaxation rates of different lipid segments are taken from paper **II** for lipids in a liquid crystalline phase. (**D**) Schematic view of the signal attenuation in the frequency domain for different lipid segments due to $R_{1\rho}$ relaxation rates as described in **C**.

Analysis of lipid dynamics using model-free formalism

Model-free formalism for describing the internal motion in proteins and anisotropic liquids have been independently developed by Wennerström and Halle[75] and Lipari and Szabo.[22] This type of analysis does not depend on the choice of a physical model for interpreting relaxation data obtained from NMR data, which can introduce bias,[76] but rather on the model-free parameters the order parameter S_{CH} and the effective correlation time τ_{e} which describe the anisotropy and rate of motions respectively. These quantities are then interpreted in the system specific context, for example lipid bilayers.

The parameters S and τ_{e} can be defined from $g(\tau)$, which is defined as

$$g(\tau) = \langle P_2[\mathbf{\mu}(t+\tau)\mathbf{\mu}(t)]\rangle, \tag{39}$$

where $\mathbf{\mu}$ is the unitary vector representing the C-H bond at times t and τ. For a lipid bilayer under MAS, $g(\tau)$ can be factored into[21]

$$g(\tau) = g_{\mathrm{f}}(\tau)g_{\mathrm{s}}(\tau), \tag{40}$$

where $g_{\mathrm{f}}(\tau)$ and $g_{\mathrm{s}}(\tau)$ are the contributions from fast internal motions (ps-ns) and slow, overall isotropic motions respectively. For a protein in solution, the motion that contributes to $g_{\mathrm{s}}(\tau)$ is isotropic tumbling of the entire molecule. This type of isotropic reorientation can only be achieved for lipids in bilayers through diffusion of lipids between anisotropic domains,[77] which is much slower than the tumbling of a soluble protein. If MAS is used at typical rates ω_{r} of tens of kHz, the sample spinning also contributes to $g_{\mathrm{s}}(\tau)$

$$g_{\mathrm{s}}(\tau) = \exp(-\tfrac{\tau}{\tau_s})\left[\tfrac{2}{3}\cos(\omega_{\mathrm{r}}\tau) + \tfrac{1}{3}\cos(\omega_{\mathrm{r}}\tau)\right], \tag{41}$$

where τ_{s} is the correlation time of the slow isotropic motions. The correlation time for the fast internal motions can be written in reduced form as

$$g'_{\mathrm{f}}(\tau) = \tfrac{g_{\mathrm{f}}(\tau)-S^2_{\mathrm{CH}}}{1-S^2_{\mathrm{CH}}}. \tag{42}$$

For lipid bilayers $g(\tau)$ typically decays rapidly from fast anisotropic motions and reaches a plateau value of S^2_{CH}, before starting to decay towards zero due to slow motions on time scales well above μs. The link between $g(\tau)$ and the experimentally observed NMR relaxation constants is provided by the spectral density function $j(\omega)$, which is the Fourier transform of $g(\tau)$

$$j(\omega) = 2\int_0^\infty \cos(\omega\tau)g(\tau)\mathrm{d}\tau. \tag{43}$$

The spectral density can be expressed as a function of $g_{\mathrm{s}}(\tau)$ and $g'_{\mathrm{f}}(\tau)$ above as[78]

$$j(\omega) = 2(1-S^2_{\mathrm{CH}})\int_0^\infty \cos(\omega\tau)g'_{\mathrm{f}}(\tau)g_{\mathrm{s}}(\tau)\mathrm{d}\tau + S^2_{\mathrm{CH}}j_s(\omega), \tag{44}$$

where $j_s(\omega)$ is the spectral density of $g_{\mathrm{s}}(\tau)$. When the fast and slow motions are well-separated in time, that is $g'_{\mathrm{f}}(\tau)$ decays to zero in less than 1 μs and $g_{\mathrm{s}}(\tau)$ starts to decay well above μs, Eq. 44 can be simplified to

$$j(\omega) = 2(1-S^2_{\mathrm{CH}})\int_0^\infty \cos(\omega\tau)g'_{\mathrm{f}}(\tau)\mathrm{d}\tau \tag{45}$$

since $g_s(\tau)$ is equal to unity and $j_s(\omega)$ is close to zero at frequencies on the order of MHz. Eq. 45 thus shows that the R_1 relaxation constant depends only on the fast internal motions. The relationship to slow motions at experimentally available spin-lock frequencies ω_1 used to measure the $R_{1\rho}$ relaxation constant (10-100 kHz) can be expressed as

$$j(\omega_1) = 2\left(1 - S_{\mathrm{CH}}^2\right)\tau_{\mathrm{e}} + S_{\mathrm{CH}}^2 j_s(\omega_1), \tag{46}$$

where the effective correlation time τ_{e} is defined as

$$\tau_e = \int_0^\infty g_{\mathrm{f}}'(\tau)\mathrm{d}\tau. \tag{47}$$

Eq. 46 applies since $\cos(\omega_1\tau)$ and $g_s(\tau)$ are approximately equal to unity on the time scale of the internal motions. The relationship between τ_{e} and experimentally determined relaxation rates can be derived from the dependence of the ^{13}C $R_{1\rho}$ and R_1 relaxation constants on the spectral density j

$$R_1 = \frac{d_{\mathrm{CH}}^2 N_{\mathrm{H}}}{20}\left[j(\omega_{\mathrm{H}} - \omega_{\mathrm{C}}) + 3j(\omega_{\mathrm{C}}) + 6j(\omega_{\mathrm{C}} + \omega_{\mathrm{H}})\right] \tag{48}$$

and

$$R_{1\rho} = \frac{d_{\mathrm{CH}}^2 N_{\mathrm{H}}}{40}\left[4j(\omega_1) + j(\omega_{\mathrm{H}} - \omega_{\mathrm{C}}) + 3j(\omega_{\mathrm{C}}) + 6j(\omega_{\mathrm{H}}) + 6j(\omega_{\mathrm{C}} + \omega_{\mathrm{H}})\right], \tag{49}$$

where d_{CH}^2 is the square of the C-H dipolar coupling constant, N_{H} is the number of bonded ^{1}H and ω_{H} and ω_{C} are the ^{1}H and ^{13}C Larmor frequencies. Under the conditions and assumptions above, τ_{e} can be approximated as

$$\tau_{\mathrm{e}} = \frac{5R_{1\rho} - 3.82R_1}{d_{\mathrm{CH}}^2 N_{\mathrm{H}}(1 - S_{\mathrm{CH}}^2)}, \tag{50}$$

which is the expression that was used to calculate τ_{e}-values from NMR experiments in papers **II** and **III**.

^{31}P Chemical shift anisotropy of lipids

The ^{31}P nucleus is a sensitive (high natural abundance, moderate-γ) probe of structure and dynamics of phospholipid headgroups. Lipids in liquid crystals are highly dynamic, but their whole-molecule motions (axial rotation and wobble) are anisotropic due to the hydrophilic-hydrophobic alignment in a bilayer. Through the

orientation dependence of the chemical shift tensor, different self-assembled lipid phases can be identified from the line shape (Fig. 17).[79] In small vesicles where lipids can reorient rapidly in all possible directions relative to $\mathbf{B}_0$, the chemical shift is averaged on the time scale of the NMR experiment which gives a peak at the isotropic chemical shift (Fig. 17A) which is the average of the chemical shift tensor principal components

$$\delta_{\mathrm{iso}} = \tfrac{1}{3}(\delta_{\mathrm{xx}} + \delta_{\mathrm{yy}} + \delta_{\mathrm{zz}}), \tag{51}$$

where

$$|\delta_{\mathrm{zz}} - \delta_{\mathrm{iso}}| \geq |\delta_{\mathrm{xx}} - \delta_{\mathrm{iso}}| \geq \left|\delta_{\mathrm{yy}} - \delta_{\mathrm{iso}}\right| \tag{52}$$

following the convention of Haeberlen.[80] In the case of lipids arranged in a cylindrical geometry of a hexagonal phase (Fig. 17B), lipids are reoriented by lateral diffusion around the symmetry axis instead of isotropically as in the case of vesicles. This leads to increased motional averaging and a corresponding decrease in the CSA which for lipids arranged in bilayers is expressed as

$$\Delta\sigma = \sigma_{\parallel} - \sigma_{\perp}, \tag{53}$$

where $\sigma_{\parallel}$ and $\sigma_{\perp}$ are the principal components parallel and perpendicular to the bilayer normal when axial symmetry leads to $\delta_{\mathrm{yy}} = \delta_{\mathrm{xx}}$. The value of $\Delta\sigma$ is related to the principal components as

$$\Delta\sigma = \tfrac{3}{2}\delta_{\mathrm{aniso}}, \tag{54}$$

where

$$\delta_{\mathrm{aniso}} = \delta_{\mathrm{zz}} - \delta_{\mathrm{iso}}. \tag{55}$$

In a lamellar phase, the only mechanism for motional averaging of the CSA is axial rotation because the lamellae have no spontaneous curvature. This leads to a further increase in the CSA as compared to a vesicle or hexagonal and gives a characteristic powder pattern with a high-frequency shoulder and low-frequency peak (Fig. 17C).

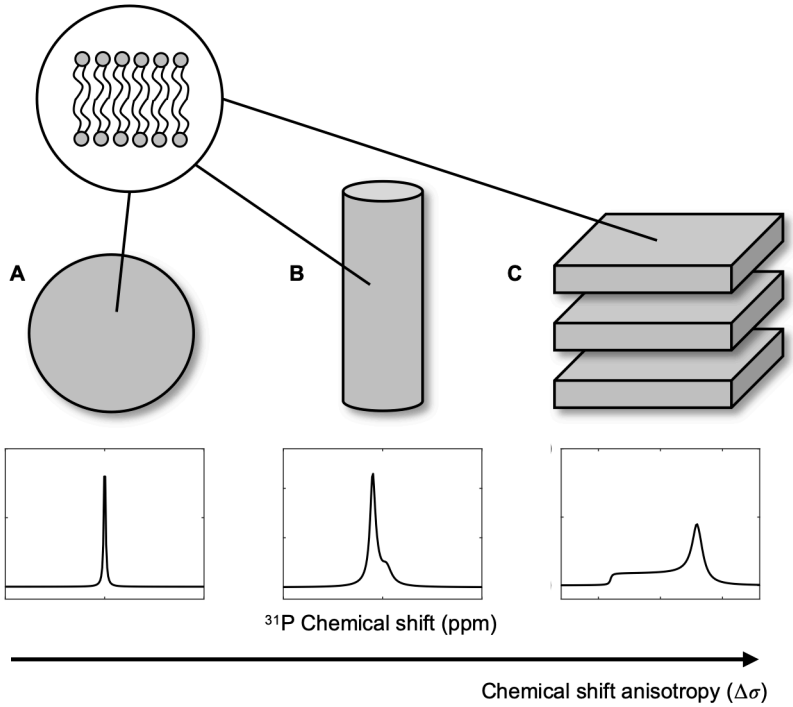

Figure 17
^{31}P Chemical shift anisotropy of different lipid phases. (**A**) The line shape of an isotropic phase such as lipids dissolved in organic solvent or vesicles with very small radii dispersed in water. Because of rapid isotropic reorientation, the CSA is averaged out which is reflected in a narrow and symmetric line. (**B**) When reorientation is constrained to diffusion on a cylinder, the isotropic averaging in **A** becomes incomplete. The incomplete averaging leads to a pattern with a high-ppm peak and a low-ppm shoulder which is characteristic for lipids arranged in a hexagonal phase. (**C**) When lipids are arranged in a lamellar phase without curvature, the only mechanism for motional averaging is rotation along the long axis of lipid molecules. This situation leads to greater chemical shift anisotropy and line shapes with a high-frequency shoulder and low-frequency peak. The theoretical value of $\Delta\sigma$ for **B** compared to **C** differs by a factor -1/2.[79]

DNP-enhanced, spin diffusion HETCOR experiments

The phenomenon of spin diffusion[81] allows polarization transfer between spatially separated spins mediated by dipolar coupling in solids, similarly to the nuclear Overhauser (NOE) effect in liquids. This can be used to investigate the spatial proximity of spins using 2D NMR.

A dynamic nuclear polarization (DNP)[82] enhanced pulse sequence based on the principle of spin diffusion was used in an attempt to detect contacts between lipids and αSyn in paper **IV**. DNP is based on polarization transfer from electrons to nuclei by irradiating unpaired electrons of in the solvent with microwaves at low temperatures.[83] This allows signal enhancements of up to a factor γ_e/γ_n, that is the gyromagnetic ratio of the electron to that of the nucleus, which is around 660 in the case of ^{1}H. The pulse sequence is shown in Fig. 18. During the first period τ_{DNP},

polarization is transferred from a radical to ^{1}H of glycerol and water molecules in the solvent and to other ^{1}H within a range on the order of 100 nm. During t_1 homonuclear eDUMBO decoupling is applied on the ^{1}H channel. During the spin diffusion mixing time τ_{SD}, spin diffusion takes place between all ^{1}H in the sample through dipolar coupling. Lastly, ^{1}H polarization is transferred to ^{13}C via CP and recorded under heteronuclear decoupling. This sequence will yield a 2D spectrum with correlation peaks between dipolar coupled nuclei on a length scale defined by τ_{SD} that can be extracted from the peak volume build-up using a rate matrix approach.[84]

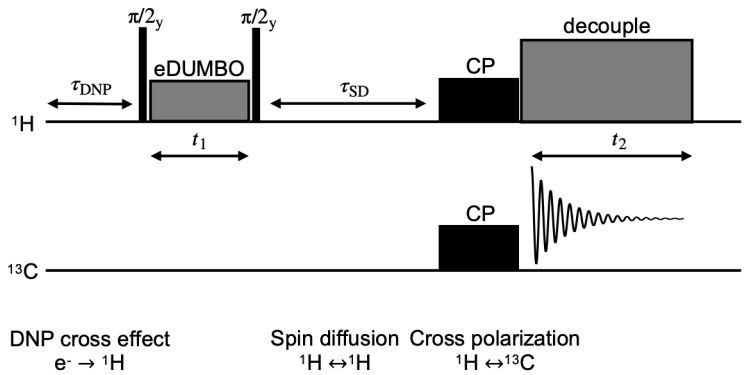

Figure 18
The DNP enhanced spin-diffusion HETCOR experiment. During τ_{DNP} polarization is transfered from electrons of a radical in the solvent to ^{1}H in the solvent. This is followed by heteronuclear ^{1}H-^{1}H eDUMBO decoupling during an $t_1$increment and spin diffusion polarization transfer between ^{1}H in the solvent and solute (target molecule) during the spin diffusion mixing time τ_{SD}. ^{1}H-^{1}H spin diffusion also occurs during τ_{DNP} and the CP block. Lastly the polarization is transferred from ^{1}H to ^{13}C within the target molecule and a FID is recorded on the ^{13}C channel. After 2D Fourier transformation, the build-up of the correlation peak volume can be related to the distance involved in the spin diffusion process using a rate matrix approach.

Co-aggregation of ganglioside GM3 and α-synuclein

This chapter aims to recapitulate the research questions and summarize the work done and main findings contained in the papers. The combined findings, their implications and limitations are then discussed separately in the conclusions section.

Composition of lipid-αSyn co-aggregates

In paper **I** we aimed to answer the question of what composition co-aggregates with αSyn and lipids have. A mixed aggregate of αSyn and lipids will likely have properties that are intermediate between the protein and lipid components, depending on their relative proportions. As such, the aggregate composition could have effects on the thermodynamic stability of aggregates and tune their interactions with other macromolecules. The relative proportions of different lipids in a co-aggregate with αSyn could also indicate if there is a preferential uptake of certain lipid species. An uptake of lipids implies that lipids are extracted from the membrane, which could affect the stability of the membrane and possibly be a toxic mechanism in Parkinson's disease. As an example, confocal microscopy experiments have shown how interaction of αSyn and vesicles containing a mixture of POPC and POPG leads to disintegration of vesicles and formation of amyloid rich lipid-protein aggregates, a process that coincides with release of fluorescent dye originally contained in the vesicles.[85]

We used a model system consisting of monomeric αSyn in the presence of SUVs containing POPC and GM3 at pH 5.5 and low ionic strength. Vesicles containing 10 or 30 mol% GM3 were added to 0.1 mM αSyn at lipid-to-protein ratios between 1 and 20, which led to spontaneous formation of aggregates during one week at 310 K (Fig. 19). The resulting precipitates were isolated from the remaining solutions by centrifugation and transferred to MAS rotors. We then measured the quantity of lipids to αSyn and the dynamics in co-aggregates using direct polarization, CP and INEPT ^{13}C MAS NMR. The remaining solutions above the precipitated aggregates were isolated, dried and dissolved in organic solvent for quantitative ^{1}H NMR analysis of the fraction of lipids that did not co-aggregate with αSyn. As reference

samples for the ^{13}C MAS NMR experiments we used equilibrium phases of the lipid system in 80 wt% buffer as well as αSyn aggregates formed in the absence of lipids.

We confirmed that aggregates contained cross-β structure characteristic for amyloid fibrils using X-ray scattering. In the complementary results from NMR analysis on the aggregates and the corresponding supernatants, we found that the fraction of lipids in aggregates increases with both the GM3 content of vesicles and the total lipid-to-protein ratio. The quantitative ^{1}H NMR also showed that the GM3-to-POPC ratio in the supernatant changes after co-aggregation with αSyn, which may suggest preferential uptake of GM3 over POPC. We also found a difference in dynamics for lipids in aggregates. The CP to INEPT ratio was increased for carbons in the GM3 headgroup, hydrophilic-hydrophobic interface region of POPC and the middle acyl chain of both lipids, which indicates that either $|S_{CH}|$ or τ_c has increased.[21] We investigated the aggregate morphology using cryo-TEM and could observe large µm-sized aggregates of fibril fragments and lipid vesicles. While the NMR results indicate that aggregates formed in the presence of 30 mol% GM3 vesicles contain a larger fraction of lipids than those from 10 mol% GM3 vesicles, fewer aggregate-adsorbed vesicles could be observed for the former using cryo-TEM. The absence of vesicles implies that they have been destabilized, while lipids are still present in the aggregates. The lipids may have been deposited as bilayers on the fibril surface or been incorporated in the fibril structure. The fact that vesicles are absent for the 30 mol% GM3 sample suggests that the interaction between vesicle and αSyn is stronger, possibly due to higher net negative membrane charge, which may promote the spreading of lipid bilayers on the αSyn surface.

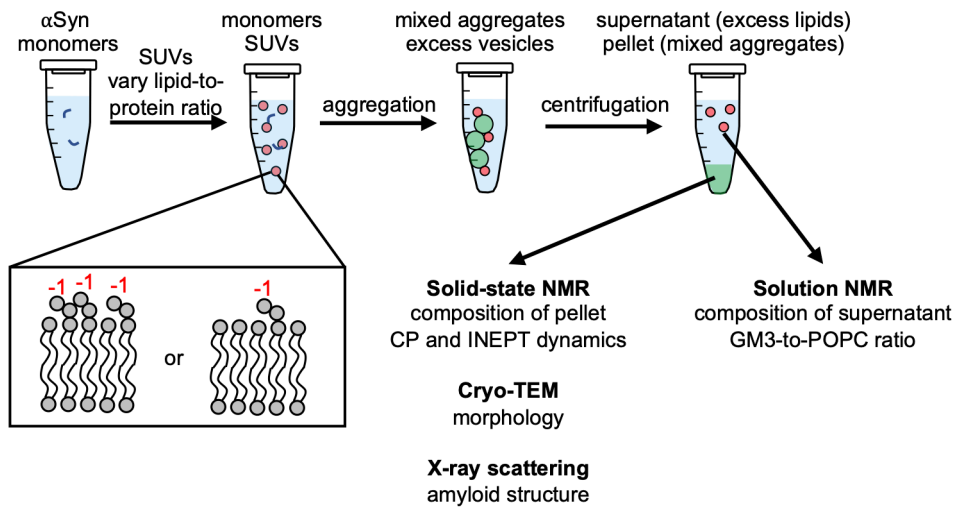

Figure 19
Graphical summary of paper **I**. The aggregation of αSyn monomer in the presence of POPC bilayers containing 10 or 30 mol% GM3 was investigated as a function of the total lipid-to-protein ratio at pH 5.5. The lipid-to-protein ratio in the

pellet and corresponding supernatants was determined by solid- and solution state NMR, while the aggregate morphology and amyloid structure weree investigated with cryo-TEM and X-ray scattering.

Structure and dynamics of the POPC-GM3 membrane

In paper **II** we addressed the question of how the lipid dynamics and order in a POPC membrane is affected by the presence of the ganglioside GM3. The study of the POPC-GM3 lipid system is an important step in the thesis work and was carried out to add context to how the more complex POPC-GM3-αSyn system behaves during the work with paper **III**. The structure of gangliosides includes a large, hydrophilic oligosaccharide headgroup that can be expected to have a large effect on the hydrophilic headgroup layer of a mixed membrane. In biological membranes the role of gangliosides is related to surface recognition of cells and proteins,[25, 86] a role where the characteristics of the headgroup layer likely important.

We used a model system consisting of an equilibrium phase of POPC with 30 mol% GM3 in 50 wt% water, for which we measured residual dipolar couplings and $R_{1\rho}$ and R_1 relaxation constants. These observables were combined to yield values of the effective correlation time τ_e, which is interpreted in terms of slow-down or acceleration of C-H bond rotation. Similar results have been obtained for pure POPC and POPC-cholesterol model systems in the past,[19, 78] which show that it is possible to obtain highly detailed information on the molecular dynamics of lipid mixtures using this approach. The model system uses GM3 which is one of the simpler gangliosides, which facilitates comparison with MD simulations. We performed 1000 ns simulations for POPC with and without GM3 and extracted independent values of $|S_{CH}|$ and τ_e for comparison with the NMR experiments.

The results from this work clearly shows the hierarchy of time scales in the dynamics of the POPC-GM3 bilayer (Fig. 20). Small groups near the end of the lipids like the choline and terminal chain methyls give τ_e on the order of 0.1 ns in NMR experiments, the central carbons of acyl chains around 2 ns and the GM3 headgroup around 20 ns at 303 K. Values of τ_e were typically larger from MD simulations, but in overall good agreement with NMR results which allowed us to gain a more complete picture than with NMR alone as the simulation is not limited by resolution or sensitivity. A gradient in $|S_{CH}|$ which is highest in the hydrophilic-hydrophobic interface region and decreases towards the end of the NeuAc residue was seen for the GM3 headgroup and increased values of τ_e was found in all parts of POPC when in the presence of GM3.

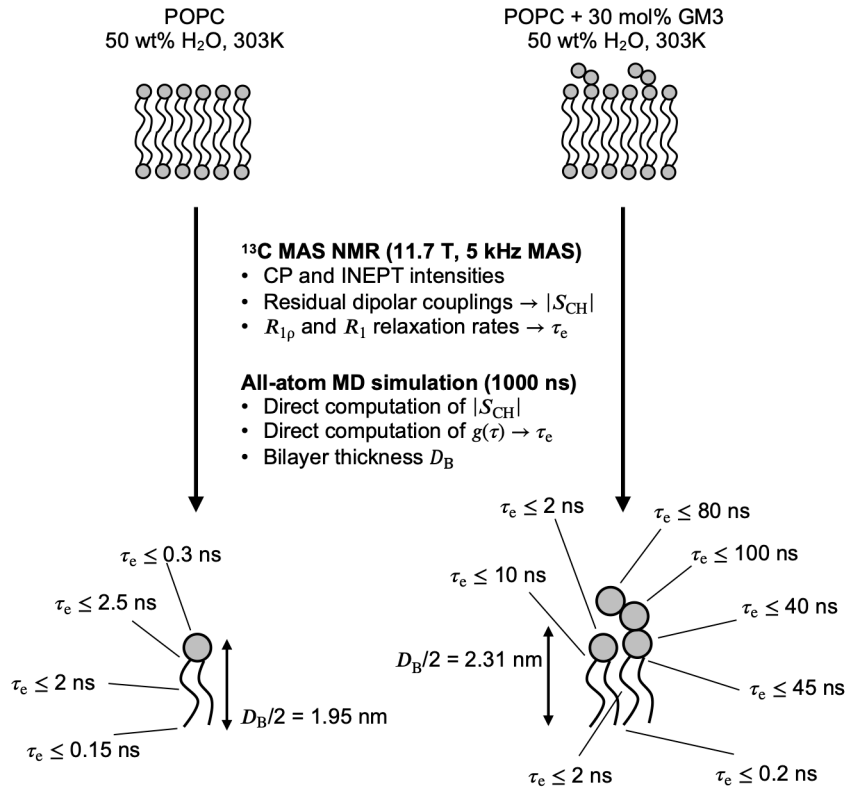

Figure 20
Graphical summary of paper **II**. NMR experiments and MD simulations were used to obtain effective correlation times τ_e for a POPC bilayer with and without 30 mol% GM3.

Structure and dynamics of lipids in co-aggregates

In paper **III** we investigated how lipids are organized in αSyn aggregates that has formed in the presence of the POPC-GM3 lipid system (Fig. 21). We approached this question by determining how the atomic-scale structure and dynamics of lipids are affected in the presence of αSyn. Previous work using POPC:POPS 7:3 showed with cryo-TEM that lipids can co-aggregate with αSyn at mildly acidic pH, disrupt the bundling of fibrils and adsorb to the surface of fibrils as deformed vesicles depending on the lipid-to-protein ratio.[6] In this case of POPC-POPS it was hypothesized based on changes in dynamics from CP and INEPT NMR experiments that lipids are likely organized as adsorbed mono- or bilayers, interior or exterior in the fibril bundling. Such a coating of lipids could have important consequences for the thermodynamic and colloidal stability of aggregates, or for the interaction

between the aggregate and other biomolecules. An adsorbed layer containing GM3 could have a large effect on the surface properties considering the role of gangliosides as surface recognition molecules.

We used the model-free analysis approach described above for paper **II** combined with measurements of the ^{31}P CSA by spinning sideband analysis.[61] The model system is the same as in paper **I**, with the exception that we used a fixed 30 mol% GM3 in vesicles at a lipid-to-protein ratio of 10. The aggregates were isolated from the remaining solution by centrifugation, dried under a stream of nitrogen and rehydrated with 50 wt% water before transferring the samples to MAS rotors. As a reference sample we used an equilibrium phase of the lipid system in 50 wt% water.

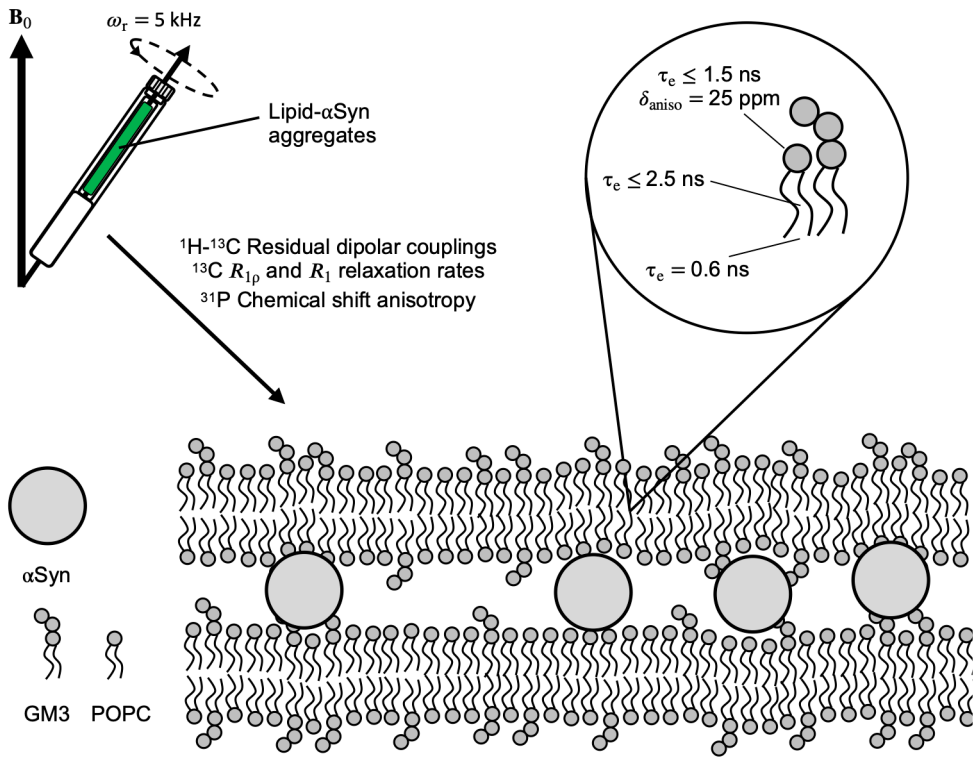

Figure 21
Graphical summary of paper **III**. Lipid-protein aggregates formed from αSyn monomers and POPC-GM3 SUVs at a lipid-to-protein ratio of 10 at pH 5.5 were studied with solid-state NMR. Effective correlation times τ_e and the chemical shift anisotropies were determined and compared between of a pure POPC-GM3 reference sample and the lipid fraction in aggregates. In the presence of αSyn, lipids have longer τ_e than in a pure lipid phase and bilayers may be deformed by intercalated fibrils.

The results from this study show that mainly the $R_{1\rho}$ relaxation rate of lipids is affected by co-aggregation with αSyn. The $R_{1\rho}$-factor in Eq. 50 typically dominates

the value of τ_e, which leads to a 3-fold increase in τ_e when lipids are aggregated with αSyn. No major changes in $|S_{CH}|$ or R_1 relaxation rates were observed for lipids in the aggregates. Obtained values of the ^{31}P CSA were 15% lower for lipids in aggregates than for the pure lipid phase. Decreased CSA indicates that POPC headgroups can reorient more isotropically in the presence of αSyn and may be caused by deformations of the bilayer in proximity to αSyn fibrils.

Conclusions

This section will summarize the most important findings of the thesis work and briefly discuss their implications and limitations. A graphical summary of the combined results is shown in Fig. 22. By using NMR, cryo-TEM and X-ray scattering experiments and MD simulations we obtained structural and dynamic information of the POPC-GM3 in the absence and presence of αSyn aggregates at mildly acidic pH.

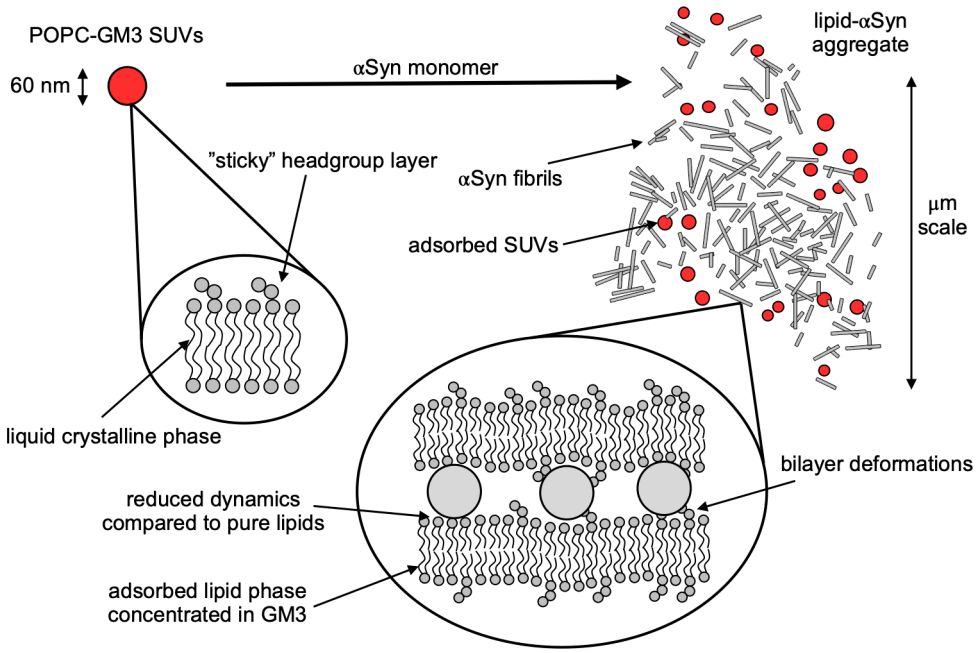

Figure 22
Graphical summary of the main findings from studies on the pure POPC-GM3 and aggregated POPC-GM3-αSyn systems. In the presence of POPC-GM3 vesicles at pH 5.5, αSyn monomers formed μm-scale aggregates that contain fibrils fragments, POPC and GM3. The properties of the lipid fraction in aggregates and reference samples with the pure lipid phase were investigated with NMR spectrocopy, while MD simulations provided synergistic information for the pure lipid phase. The morphology of the aggregates and stucture of fibrils were investigated using cryo-TEM and X-ray scattering.

Properties of the POPC-GM3 system

From the experiments on the pure lipid system, the main findings are:

1. The most prominent feature of the POPC-GM3 bilayer is the high values of $|S_{CH}|$ and τ_e in the GM3 hydrophilic-hydrophobic interface and headgroup layer.
2. The presence of GM3 increases $|S_{CH}|$ and τ_e in all segments of POPC.

Gangliosides are surface recognition molecules that are present on the outer leaflet of cell membranes where they can interact with other macromolecules. Gangliosides are distinguished by their large hydrophilic oligosaccharide headgroups and the properties of the headgroup can be expected to form a part of the basis for how gangliosides perform their functions. The values of $|S_{CH}|$ and τ_e that we measured are useful in understanding how gangliosides behave as membrane components and how they influence the properties of a mixed membrane. The $|S_{CH}|$ and τ_e-values can also be useful in future studies to gain mechanistic information in how ganglioside membranes interact with other molecules such as proteins. The high order in the GM3 headgroup is likely related to the well-known conformational rigidity of the pyranose rings. The values of τ_e for the GM3 headgroup are 6-7 times longer than for the slowest segments in POPC. The longer τ_e for GM3 indicates that tumbling of the headgroup which occurs on the ns time scale for POPC is slower for GM3 which can be related to the size of the oligosaccharide moiety.

The increase of τ_e for POPC in the presence of GM3 shows how gangliosides can affect the properties of a mixed membrane. Gangliosides have higher melting points than POPC due to the fully saturated middle of the hydrophobic tails. Saturated hydrocarbons have stronger interchain interactions than unsaturated hydrocarbons and could lead to the observed increase in τ_e in the presence of GM3.

Properties of POPC-GM3-αSyn aggregates

For the lipid-αSyn aggregates, the main findings are:

1. Large μm-sized amorphous aggregates are formed that contain both POPC and GM3.
2. The aggregates are collections of short amyloid fibrils, lipid vesicles and adsorbed bilayers.
3. Longer τ_e leads to increased $R_{1\rho}$ rates lead to for lipids in aggregates compared to a pure lipid phase.

The morphology of αSyn aggregates is highly dependent on the solution conditions and the sample preparation protocol. At neutral and high pH, αSyn fibrils are

colloidally stable due to electrostatic repulsion, while at mildly acid pH fibrils stick together in bundles.[87] The aggregates we observed using cryo-TEM seems to be formed from short fibril fragments, which have condensed into large amorphous aggregates. Fragmentation is likely a consequence of the mechanical stirring or the sonication used to redisperse aggregates before cryo-TEM imaging. When fragmentation occurs, it may catalyse the growth of fibrils by creating new ends where monomers can add to the existing fibrils. αSyn fibrils have a negative ζ-potential at pH 5.5, comparable to a SUV containing 30 mol% anionic DOPS,[28] which means that there is a repulsive electrostatic force between fibrils with a range described by the Debye length which is ca 3 nm in the 10 mM MES buffer we use. However, due to the uneven charge distribution in αSyn, electrostatic interactions can be important in promoting aggregation where the positive N-terminus is attracted to the negative C-terminus[41] and lipid membranes with anionic lipids.

In cryo-TEM images we can observe vesicles adsorbed to fibril aggregates, but we cannot resolve adsorbed bilayers. However, it is possible that vesicles have spread on the fibril surfaces, which would substantially alter the surface properties compared to a pure αSyn system and implies that vesicles have been destabilized. From both quantitative ^{13}C and ^{1}H NMR experiments we can conclude that there is a large fraction of lipids in aggregates formed from 30 mol% GM3 vesicles, where few or no adsorbed vesicles can be observed using cryo-TEM. In the corresponding ^{31}P NMR powder spectra the line shape is characteristic for a lamellar phase, with line broadening indicating reduced dynamics compared to the pure lipid sample.

If there is a thermodynamic driving force for spreading of vesicles on fibrils, this implies that the surface free energy of the fibril-water surface is greater than the sum of the fibril-bilayer and bilayer-water surface energies, neglecting changes in conformational entropy of the rigid fibril structure. This balance of surface energies is reasonable considering that i) αSyn is close to the isoelectric point (4.7) at pH 5.5, which may lead to a relatively high surface energy depending on what parts of the protein that are exposed to the bulk solution, and ii) the lipid headgroup-water surface energy is likely lower than for some parts of αSyn, which contains a mixture of apolar and polar residues.

The τ_e-values are on average three times longer for lipids in aggregates compared to a pure lipid phase, which leads to increased $R_{1\rho}$ rates while R_1 rates and $|S_{CH}|$ are unchanged. The likely mechanism behind longer τ_e is that whole-lipid motions such as axial rotation and wobble becomes slower, which shifts the associated region in $g(\tau)$ from the 10 ns time scale to 30 ns. It is also possible that the presence of αSyn can deform the lipid bilayer in some way, which causes a slight decrease in the ^{31}P CSA, however this is unlikely given the unchanged $|S_{CH}|$ values.

The role of ganglioside GM3 in co-aggregation

From the studies where we varied the amount of GM3 in the system, the main findings are:

1. Using 30 mol% GM3 vesicles leads to a larger fraction of lipids in aggregates compared to 10 mol% GM3 vesicles.
2. Uptake of lipids is slightly selective for GM3 over POPC.

Gangliosides GM1 and GM3 have been shown to increase the rate of αSyn aggregation more than other negatively charged lipids.[27] The GM3 headgroup stripped of the hydrophobic ceramide moiety was also found to increase the rate of αSyn aggregation without any changes in αSyn secondary structure normally associated with binding of the αSyn monomer to lipid membranes. Our results suggest that GM3 is also able to affect the thermodynamics of aggregate formation, which controls the composition of aggregates.

For amphipathic proteins, binding to lipid membranes is generally driven by an exothermic change in enthalpy associated with hydrophobicity of the molecules, electrostatic interactions and hydrogen bonding.[88] GM3 has an oligosaccharide headgroup which is predisposed for hydrogen bonding and has a net negative charge compared to the zwitterionic POPC. These two factors may cause the interaction between 30 mol% GM3 vesicles and αSyn to be more favorable than for 10 mol% GM3 vesicles, leading to a higher lipid uptake at the higher GM3 content. From the CP and INEPT intensities for lipids in αSyn aggregates in papers **I** and **III** we can observe that the POPC headgroup segments give INEPT but no CP, and for the GM3 headgroup segments the situation is opposite. This means that POPC can reorient isotropically on the time scale of less than 10 ns, while the GM3 headgroup may experience slower dynamics due to a stronger interaction with αSyn. The findings in paper **II** also shows that the GM3 headgroup has a "sticky" character, with high values of τ_e and $|S_{CH}|$ which may promote interaction with αSyn. A selective uptake suggests that lipids are extracted from the membrane with unequal probabilities. This could be related to a stronger interaction between GM3 and αSyn or higher water solubility of GM3 compared to POPC.

DNP-enhanced spin-diffusion HETCOR experiments

During the thesis work we used the experiment described in Fig.18 in an attempt to detect spatial contacts and model intermolecular distances between lipids and αSyn in aggregates. In paper **IV** another lipid-protein system; stratum corneum (upper layer of skin) was investigated with the same HETCOR technique. Fig. 23 shows preliminary data acquired on the POPC-GM3-αSyn system with this technique, however in contrast to the stratum corneum data the resolution under DNP-conditions is too low to detect any lipid-αSyn contacts. Because of the low

resolution, the POPC-GM3-αSyn data was not included in paper **IV**. The following paragraph will describe the challenges in using these HECTOR experiments and how conditions may be optimized to provide information on the POPC-GM3-αSyn system in the future.

The DNP-enhanced spin-diffusion HETCOR experiments require careful selection of the delays which control the DNP, spin diffusion and CP build-up to find a combination of delays which correspond to an observable correlation peak between lipid and protein in the 2D spectrum. At the conditions of our DNP-enhanced experiments where the sample is suspended in a glassy matrix of glycerol and water at 100 K, the resolution is too low (Fig. 23) to detect any correlation peaks between lipids and αSyn. In the corresponding spectra without DNP, signal-to-noise it typically low and we were unable to detect any correlation peaks between lipids and αSyn. The mechanism behind the low resolution in the DNP experiments is that in the frozen DNP-solvent, molecules are trapped in different conformations representing the entire conformational ensemble, where many molecular motions are suspended and unable to average out the corresponding distribution of chemical shifts.[89] The structure of our type of aggregate sample is composed of large collections of seemingly randomly oriented fibril fragments with adsorbed intact lipid vesicles and possibly bilayers adsorbed on fibril surfaces. The resolution can be expected to improve if experiments are performed at higher temperatures, where motional averaging is more pronounced. It may also be possible to optimize the solvent composition by changing the glycerol-to-water ratio or with some additive, to promote a different glass structure where the distribution of available molecular conformations is narrower. It may also be possible to modify the sample preparation protocol by excluding the sample mixing with mechanical stirring to produce a less polydisperse distribution of fibrils.

The main finding from the DNP-enhanced experiments is that the resolution is too low to observe any lipid-αSyn correlation peaks, which precluded further analysis on the molecular structure. Future directions for this type of experiments are suggested in the outlook section.

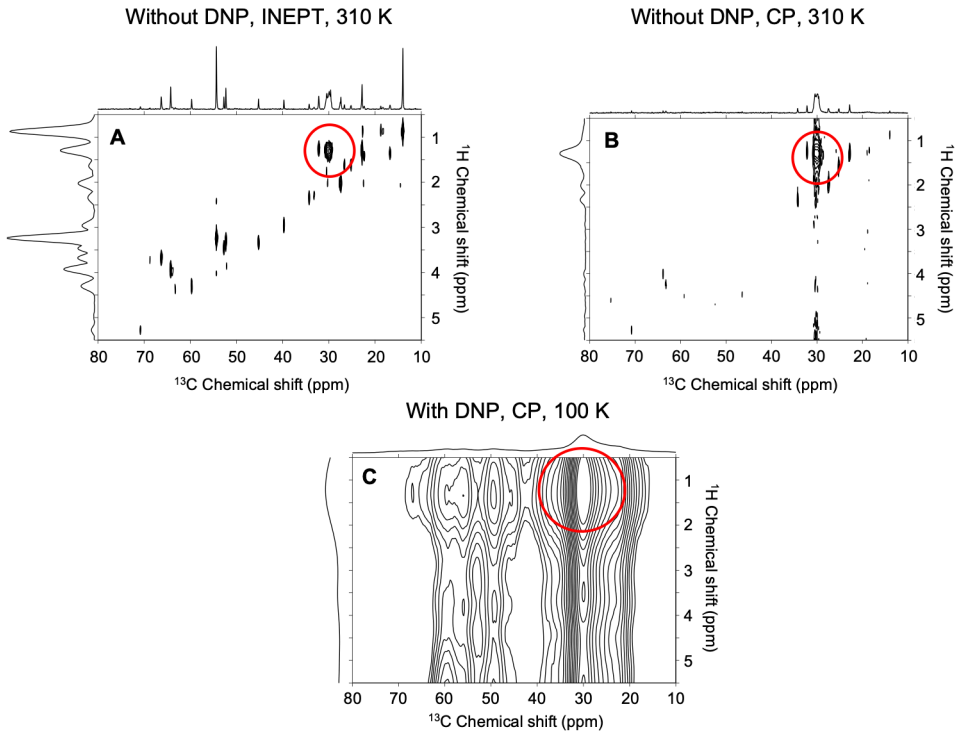

Figure 23
Comparison of resolution in spin-diffusion ^{1}H-^{13}C HETCOR spectra for measurements on lipid-αSyn aggregates under conventional and DNP-conditions. The spectra in (**A**) and (**B**) were acquired without DNP on a sample in water at 310 K, with INEPT and CP for ^{1}H-^{13}C polarization transfer respectively. The spectrum in (**C**) was acquired with DNP on a sample in glycerol/water at 100 K, with CP for ^{1}H-^{13}C polarization transfer. As an example of the line broadening, the red circles mark the signal from the central carbons of the lipid acyl chains in all spectra.

Present findings placed in a broader perspective

The model system that we used to study co-aggregation was composed of SUVs and αSyn monomers at mildly acidic pH (5.5) and low ionic strength (10 mM MES) conditions and at a low lipid-to-protein molar ratios (from 1 to 20). At these conditions, primary nucleation is enhanced by lipid surfaces and αSyn monomers rapidly grow into fibrils from a mixture of secondary nucleation, elongation and fragmentation. At pH 5.5 secondary nucleation dominates over elongation and because we used mechanical stirring, we promoted growth via fragmentation of fibrils. This means that aggregates form rapidly under these conditions and precipitates were often observed after 2-3 days. However, samples were allowed to continue aggregate for a full week to reach a kinetic steady-state which was subsequently analyzed using the experimental techniques. These conditions are

relevant to cellular compartments with locally reduced pH, such as lysosomes and endosomes.[28, 90] We should be careful when trying to generalize our conclusions outside of this model system because of the large effect of solution conditions on the structure of aggregates.[39] However, studies that use experimental approaches similar to ours show that the lipid-αSyn co-aggregation behavior in terms of lipid dynamics and structure is comparable also at pH 6.5 and with other lipid systems.[4, 6]

As a membrane model we used lipid mixtures of POPC with 10 or 30 mol% GM3. POPC is ubiquitous in biological membranes, while GM3 predominates the outer leaflet of many peripheral tissues such as heart, kidney, liver and adipose tissue. GM3 is one of the simpler gangliosides, with three headgroup residues compared to five for GM1. The relatively simple structure of GM3 is favorable for avoiding crowded NMR spectra, which would complicate analysis. However, we still experienced problems with resolution of some GM3 peaks, especially during the $R_{1\rho}$ and R_1 relaxation measurements that were performed as pseudo 2D experiments. These experiments could be improved by using a higher-field instrument or by deuterating αSyn, which would allow selective detection of lipid signals via CP and INEPT experiments as these depend on polarization transfer from ^{1}H to ^{13}C.

Mammalian cell membranes contain around 10 mol% anionic lipids on average,[91] but the lipid composition varies between the inner and outer leaflets of the plasma membrane and between different organelles. Using a GM3 concentration of 10 mol% leads to very low sensitivity in NMR experiments for our model system. We could have increased the signal-to-noise ratio by isotopic enrichment of ^{13}C, but this is expensive and commercially unavailable for a relatively niche lipid such as GM3.

We chose to use sonicated SUVs with ca 30 nm hydrodynamic radius as our lipid model. SUVs are a reasonable lipid model since the native environment and function of αSyn relates to synaptic vesicles which have a radius on the order of 20 nm.[92]

Outlook

During the thesis work we studied the aggregation of αSyn in the presence of POPC-GM3 vesicles. The main results and implications have been summarized in the previous chapters. Below I will give some possible directions on how to complete and build upon the results obtained during the thesis work.

Paper **I**: We measured the composition of lipid-protein aggregates which showed that the GM3 content of vesicles correlates with the amount of lipids in fibrils and that there is a selective uptake of GM3. Other studies using GM1 have indicated that there is a selective uptake of GM1[5] and our results could be complemented by measurements with other gangliosides to investigate if the observed effects are general for this type of lipids. Measurements at different solution conditions including pH, temperature and ionic strength could show what type of interactions that are most important between GM3 and αSyn.

Paper **II**: We measured $|S_{CH}|$ and τ_e for POPC bilayers containing 30 mol% GM3. By combining the results from NMR experiments and MD simulation we obtained a relatively complete picture of the atomic-scale dynamics of the lipid system. The simulated values of the bilayer dimensions could be validated by X-ray scattering experiments. Performing diffusion NMR experiments could also complement the results by adding information on the rate of lateral diffusion in the bilayer. In paper **I**, we refer to the sample as an equilibrium phase of POPC and GM3, but the distribution of potentially co-existing phases for this type of sample is not well-known. It is likely that there is a co-existence of lamellar phase and GM3 vesicles at equilibrium (depending on the water content and temperature) and this could by studied more using modelling of X-ray scattering or ^{31}P NMR CSA data, or by direct observation with cryo-TEM.

Paper **III**: We measured $|S_{CH}|$, τ_e and ^{31}P CSA for lipids in lipid-protein aggregates, which suggest that lipids are organized as adsorbed bilayers with intercalated fibrils which imposes some type of deformation on the bilayers. A more complete picture of the lipid organization could be obtained by performing additional X-ray scattering and multidimensional heteronuclear correlation NMR experiments to model the structure of the lipid-protein aggregates. Diffusion NMR experiments could also be added to investigate the dynamics in more detail. Isotopic enrichment of ^{13}C in lipids and/or perdeuteration of αSyn could be used to improve the signal-to-noise and resolution in experiments respectively.

Paper **IV**: We applied a DNP-enhanced spin-diffusion HECTOR experiment in an attempt to measure lipid-αSyn contacts in aggregates but were unable to do so in preliminary experiments. It was however possible to extract information on the stratum corneum system with the same technique. At the conditions in paper **IV** with the sample suspended in a glycerol/water mixture (DNP-juice) at 100 K, the chemical shift resolution is insufficient for observing any correlation peaks in the lipid-αSyn system. The mechanism for the low resolution is that in the frozen mixture molecules are trapped in a statistical distribution which represents the entire conformational distribution, with corresponding large peak widths which leads to overlap of signals from lipids, αSyn and glycerol/water in the spectrum. To improve the resolution, experiments could be performed at higher temperatures to enhance motional averaging, or it may be possible to optimize the composition of the solvent mixture to promote a different glass structure.

References

1. T. P. J. Knowles, M. Vendruscolo and C. M. Dobson, *Nature Reviews Molecular Cell Biology*, 2014, **15**, 384-396.
2. M. G. Spillantini, M. L. Schmidt, V. M.-Y. Lee, J. Q. Trojanowski, R. Jakes and M. Goedert, *Nature*, 1997, **388**, 839-840.
3. S. H. Shahmoradian, A. J. Lewis, C. Genoud, J. Hench, T. E. Moors, P. P. Navarro, D. Castaño-Díez, G. Schweighauser, A. Graff-Meyer and K. N. Goldie, *Nature neuroscience*, 2019, **22**, 1099-1109.
4. C. l. Galvagnion, D. Topgaard, K. Makasewicz, A. K. Buell, S. Linse, E. Sparr and C. M. Dobson, *The journal of physical chemistry letters*, 2019, **10**, 7872-7877.
5. R. Gaspar, I. Idini, G. Carlström, S. Linse and E. Sparr, *Frontiers in cell and developmental biology*, 2021, **9**, 622764.
6. E. Hellstrand, A. Nowacka, D. Topgaard, S. Linse and E. Sparr, *PloS one*, 2013, **8**, e77235.
7. D. F. Evans and H. Wennerström, *The colloidal domain: where physics, chemistry, biology, and technology meet*, Wiley-VCH, 1999.
8. O. G. Mouritsen, *Life-as a matter of fat*, Springer, 2005.
9. J. H. Ipsen and O. G. Mouritsen, *Biochimica et Biophysica Acta (BBA)-Biomembranes*, 1988, **944**, 121-134.
10. S. Ray, N. Singh, R. Kumar, K. Patel, S. Pandey, D. Datta, J. Mahato, R. Panigrahi, A. Navalkar and S. Mehra, *Nature chemistry*, 2020, **12**, 705-716.
11. A. Siegert, M. Rankovic, F. Favretto, T. Ukmar-Godec, T. Strohäker, S. Becker and M. Zweckstetter, *Protein Science*, 2021, **30**, 1326-1336.
12. C. Galvagnion, A. K. Buell, G. Meisl, T. C. Michaels, M. Vendruscolo, T. P. Knowles and C. M. Dobson, *Nature chemical biology*, 2015, **11**, 229-234.
13. H. Wennerström, E. Vallina Estrada, J. Danielsson and M. Oliveberg, *Proceedings of the National Academy of Sciences*, 2020, **117**, 10113-10121.
14. J. W. Tester and M. Modell, *Thermodynamics and its applications*, Prentice Hall PTR, 1997.
15. L. Svennerholm, *Journal of lipid research*, 1964, **5**, 145-155.
16. J. N. Israelachvili, D. J. Mitchell and B. W. Ninham, *Journal of the Chemical Society, Faraday Transactions 2: Molecular and Chemical Physics*, 1976, **72**, 1525-1568.

17. S. Sonnico, D. Acquotti, M. Corti and G. Tettamanti, *Chemistry and physics of lipids*, 1990, **52**, 231-241.
18. O. G. Mouritsen, *European journal of lipid science and technology*, 2011, **113**, 1174-1187.
19. H. S. Antila, A. Wurl, O. S. Ollila, M. S. Miettinen and T. M. Ferreira, *Biophysical Journal*, 2022, **121**, 68-78.
20. A. A. Smith, A. Vogel, O. Engberg, P. W. Hildebrand and D. Huster, *Nature communications*, 2022, **13**, 1-13.
21. A. Nowacka, P. C. Mohr, J. Norrman, R. W. Martin and D. Topgaard, *Langmuir*, 2010, **26**, 16848-16856.
22. G. Lipari and A. Szabo, *Journal of the American Chemical Society*, 1982, **104**, 4546-4559.
23. P. H. Fishman and R. O. Brady, *Science*, 1976, **194**, 906-915.
24. R. L. Schnaar, R. Gerardy-Schahn and H. Hildebrandt, *Physiological reviews*, 2014.
25. P. H. Lopez and R. L. Schnaar, *Current opinion in structural biology*, 2009, **19**, 549-557.
26. K. Palmano, A. Rowan, R. Guillermo, J. Guan and P. Mc Jarrow, *Nutrients*, 2015, **7**, 3891-3913.
27. R. Gaspar, J. Pallbo, U. Weininger, S. Linse and E. Sparr, *Biochimica et Biophysica Acta (BBA)-Proteins and Proteomics*, 2018, **1866**, 1062-1072.
28. M. Grey, C. J. Dunning, R. Gaspar, C. Grey, P. Brundin, E. Sparr and S. Linse, *Journal of Biological Chemistry*, 2015, **290**, 2969-2982.
29. R. B. Chan, A. J. Perotte, B. Zhou, C. Liong, E. J. Shorr, K. S. Marder, U. J. Kang, C. H. Waters, O. A. Levy and Y. Xu, *PLoS One*, 2017, **12**, e0172348.
30. J. Burré, *Journal of Parkinson's disease*, 2015, **5**, 699-713.
31. L. Maroteaux, J. T. Campanelli and R. H. Scheller, *Journal of Neuroscience*, 1988, **8**, 2804-2815.
32. M. H. Polymeropoulos, C. Lavedan, E. Leroy, S. E. Ide, A. Dehejia, A. Dutra, B. Pike, H. Root, J. Rubenstein and R. Boyer, *science*, 1997, **276**, 2045-2047.
33. B. Winner, R. Jappelli, S. K. Maji, P. A. Desplats, L. Boyer, S. Aigner, C. Hetzer, T. Loher, M. Vilar and S. Campioni, *Proceedings of the National Academy of Sciences*, 2011, **108**, 4194-4199.
34. M. J. Benskey, R. G. Perez and F. P. Manfredsson, *Journal of neurochemistry*, 2016, **137**, 331-359.
35. G. Fusco, S. W. Chen, P. T. Williamson, R. Cascella, M. Perni, J. A. Jarvis, C. Cecchi, M. Vendruscolo, F. Chiti and N. Cremades, *Science*, 2017, **358**, 1440-1443.
36. R. F. Roberts, R. Wade-Martins and J. Alegre-Abarrategui, *Brain*, 2015, **138**, 1642-1657.
37. A.-L. Mahul-Mellier, J. Burtscher, N. Maharjan, L. Weerens, M. Croisier, F. Kuttler, M. Leleu, G. W. Knott and H. A. Lashuel, *Proceedings of the National Academy of Sciences*, 2020, **117**, 4971-4982.

38. L. C. Serpell, J. Berriman, R. Jakes, M. Goedert and R. A. Crowther, *Proceedings of the National Academy of Sciences*, 2000, **97**, 4897-4902.
39. W. Hoyer, T. Antony, D. Cherny, G. Heim, T. M. Jovin and V. Subramaniam, *Journal of molecular biology*, 2002, **322**, 383-393.
40. A. K. Buell, C. Galvagnion, R. Gaspar, E. Sparr, M. Vendruscolo, T. P. Knowles, S. Linse and C. M. Dobson, *Proceedings of the National Academy of Sciences*, 2014, **111**, 7671-7676.
41. R. Gaspar, M. Lund, E. Sparr and S. Linse, *QRB Discovery*, 2020, **1**.
42. W. S. Davidson, A. Jonas, D. F. Clayton and J. M. George, *Journal of Biological Chemistry*, 1998, **273**, 9443-9449.
43. T. S. Ulmer, A. Bax, N. B. Cole and R. L. Nussbaum, *Journal of Biological Chemistry*, 2005, **280**, 9595-9603.
44. G. Fusco, A. De Simone, T. Gopinath, V. Vostrikov, M. Vendruscolo, C. M. Dobson and G. Veglia, *Nature communications*, 2014, **5**, 1-8.
45. C. Galvagnion, J. W. Brown, M. M. Ouberai, P. Flagmeier, M. Vendruscolo, A. K. Buell, E. Sparr and C. M. Dobson, *Proceedings of the National Academy of Sciences*, 2016, **113**, 7065-7070.
46. G. P. Gorbenko and P. K. Kinnunen, *Chemistry and physics of lipids*, 2006, **141**, 72-82.
47. K. Gade Malmos, L. M. Blancas-Mejia, B. Weber, J. Buchner, M. Ramirez-Alvarado, H. Naiki and D. Otzen, *Amyloid*, 2017, **24**, 1-16.
48. R. K. Harris, *Nuclear Magnetic Resonance Spectroscopy*, Pitman, 1983.
49. J. Keeler, *Understanding NMR spectroscopy*, John Wiley & Sons, 2011.
50. M. H. Levitt, *Spin dynamics: Basics of nuclear magnetic resonance*, John Wiley & Sons, 2008.
51. F. Bloch, *Physical review*, 1946, **70**, 460.
52. R. R. Ernst and W. A. Anderson, *Review of Scientific Instruments*, 1966, **37**, 93-102.
53. A. Bax and R. Freeman, *Journal of Magnetic Resonance*, 1981, **44**, 542-561.
54. S. Macura and R. Ernst, *Molecular Physics*, 1980, **41**, 95-117.
55. G. M. Clore and A. M. Gronenborn, *Trends in biotechnology*, 1998, **16**, 22-34.
56. K. Schmidt-Rohr, J. Clauss and H. Spiess, *Macromolecules*, 1992, **25**, 3273-3277.
57. R. F. Evilia, *Analytical Letters*, 2001, **34**, 2227-2236.
58. T. Oas, R. Griffin and M. Levitt, *The Journal of chemical physics*, 1988, **89**, 692-695.
59. R. Hester, J. Ackerman, B. Neff and J. Waugh, *Physical Review Letters*, 1976, **36**, 1081.
60. S. V. Dvinskikh, H. Zimmermann, A. Maliniak and D. Sandström, *Journal of Magnetic Resonance*, 2004, **168**, 194-201.
61. J. Herzfeld and A. E. Berger, *The Journal of Chemical Physics*, 1980, **73**, 6021-6030.

62. P. Chen, B. J. Albert, C. Gao, N. Alaniva, L. E. Price, F. J. Scott, E. P. Saliba, E. L. Sesti, P. T. Judge and E. W. Fisher, *Science advances*, 2018, **4**, eaau1540.
63. A. E. Bennett, C. M. Rienstra, M. Auger, K. Lakshmi and R. G. Griffin, *The Journal of chemical physics*, 1995, **103**, 6951-6958.
64. B. Fung, A. Khitrin and K. Ermolaev, *Journal of magnetic resonance*, 2000, **142**, 97-101.
65. S. Penzel, A. Oss, M.-L. Org, A. Samoson, A. Böckmann, M. Ernst and B. H. Meier, *Journal of biomolecular NMR*, 2019, **73**, 19-29.
66. B. Elena, G. de Paëpe and L. Emsley, *Chemical physics letters*, 2004, **398**, 532-538.
67. S. V. Dvinskikh, V. Castro and D. Sandström, *Physical Chemistry Chemical Physics*, 2005, **7**, 607-613.
68. A. Pines, M. Gibby and J. Waugh, *The Journal of Chemical Physics*, 1972, **56**, 1776-1777.
69. G. Morris and R. Freeman, *J. Amer. Chem. Soc.*, 1979, **101**, 760.
70. A. Nowacka, N. Bongartz, O. Ollila, T. Nylander and D. Topgaard, *Journal of Magnetic Resonance*, 2013, **230**, 165-175.
71. J. Becker, A. Comotti, R. Simonutti, P. Sozzani and K. Saalwächter, *The Journal of Physical Chemistry B*, 2005, **109**, 23285-23294.
72. A. Seelig and J. Seelig, *Biochemistry*, 1974, **13**, 4839-4845.
73. X. Zhao, M. Edén and M. H. Levitt, *Chemical physics letters*, 2001, **342**, 353-361.
74. D. A. Torchia, *Journal of Magnetic Resonance (1969)*, 1978, **30**, 613-616.
75. B. Halle and H. Wennerström, *The Journal of Chemical Physics*, 1981, **75**, 1928-1943.
76. A. A. Smith, M. Ernst and B. H. Meier, *Angewandte Chemie*, 2017, **129**, 13778-13783.
77. I. Åslund, C. Cabaleiro-Lago, O. Söderman and D. Topgaard, *The Journal of Physical Chemistry B*, 2008, **112**, 2782-2794.
78. T. M. Ferreira, O. S. Ollila, R. Pigliapochi, A. P. Dabkowska and D. Topgaard, *The Journal of Chemical Physics*, 2015, **142**, 044905.
79. P. t. Cullis and B. De Kruijff, *Biochimica et Biophysica Acta (BBA)-Reviews on Biomembranes*, 1979, **559**, 399-420.
80. M. Mehring, *Principles of high resolution NMR in solids*, 2012.
81. D. Suter and R. Ernst, *Physical Review B*, 1985, **32**, 5608.
82. A. Abragam and M. Goldman, *Reports on Progress in Physics*, 1978, **41**, 395.
83. T. Maly, G. T. Debelouchina, V. S. Bajaj, K.-N. Hu, C.-G. Joo, M. L. Mak–Jurkauskas, J. R. Sirigiri, P. C. Van Der Wel, J. Herzfeld and R. J. Temkin, *The Journal of chemical physics*, 2008, **128**, 02B611.
84. B. Elena and L. Emsley, *Journal of the American Chemical Society*, 2005, **127**, 9140-9146.
85. H. Chaudhary, A. N. Stefanovic, V. Subramaniam and M. M. Claessens, *FEBS letters*, 2014, **588**, 4457-4463.

86. M. L. DeMarco and R. J. Woods, *Glycobiology*, 2009, **19**, 344-355.
87. B. H. Pogostin, S. Linse and U. Olsson, *Langmuir*, 2019, **35**, 16536-16544.
88. J. Seelig, *Biochimica et Biophysica Acta (BBA)-Biomembranes*, 2004, **1666**, 40-50.
89. B. Uluca, T. Viennet, D. Petrović, H. Shaykhalishahi, F. Weirich, A. Gönülalan, B. Strodel, M. Etzkorn, W. Hoyer and H. Heise, *Biophysical journal*, 2018, **114**, 1614-1623.
90. L. Stefanis, E. Emmanouilidou, M. Pantazopoulou, D. Kirik, K. Vekrellis and G. K. Tofaris, *Journal of neurochemistry*, 2019, **150**, 577-590.
91. M. A. Lemmon, *Nature reviews Molecular cell biology*, 2008, **9**, 99-111.
92. T. C. Südhof, *Annu. Rev. Neurosci.*, 2004, **27**, 509-547.

Printed by Media-Tryck, Lund 2022 NORDIC SWAN ECOLABEL 3041 0903

ISBN: 978-91-7422-910-3

Physical Chemistry
Faculty of Science
Lund University